Article
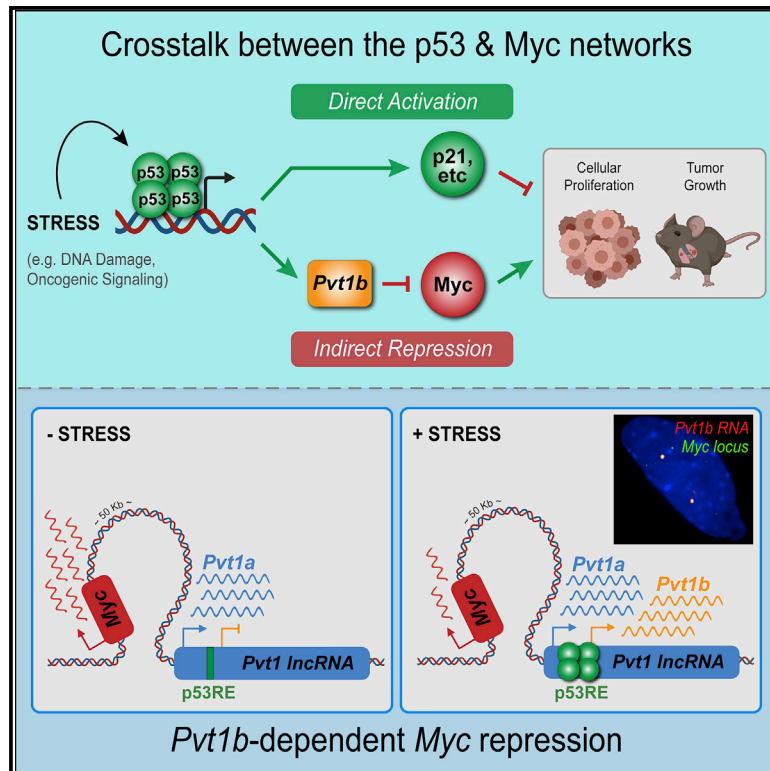
p53 Activates the Long Noncoding RNA *Pvt1b* to Inhibit *Myc* and Suppress Tumorigenesis

Graphical Abstract

Authors

Christiane E. Olivero,
Elena Martínez-Terroba,
Joshua Zimmer, ..., Matthew D. Simon,
Jesse R. Zamudio, Nadya Dimitrova

Correspondence

nadya.dimitrova@yale.edu

In Brief

Olivero et al. identify the conserved lncRNA isoform *Pvt1b* as a locus-specific transcriptional regulator that serves to repress *Myc* transcription during the p53-mediated response to stress. Production of the *Pvt1b* RNA inhibits cellular proliferation and tumor growth, revealing tumor suppressor activities for this cancer-associated lncRNA.

Highlights

- *Pvt1b* is a p53-dependent lncRNA isoform, induced by genotoxic and oncogenic stress

- Production of *Pvt1b* RNA represses *Myc* transcription in *cis*

- *Pvt1b* suppresses Myc transcriptional program and cellular proliferation

- *Pvt1b* limits tumor growth, but not tumor progression, in a mouse lung tumor model

CellPress

p53 Activates the Long Noncoding RNA *Pvt1b* to Inhibit *Myc* and Suppress Tumorigenesis

Christiane E. Olivero,[1] Elena Martínez-Terroba,[1] Joshua Zimmer,[2] Clara Liao,[1] Ephrath Tesfaye,[1] Nima Hooshdaran,[3] Jeremy A. Schofield,[2] Jordan Bendor,[1] Dorthy Fang,[1] Matthew D. Simon,[2] Jesse R. Zamudio,[3] and Nadya Dimitrova[1,4,*]

[1]Department of Molecular, Cellular, and Developmental Biology, Yale University, New Haven, CT 06511, USA
[2]Department of Molecular Biophysics and Biochemistry, Yale University, New Haven, CT 06511, USA
[3]Department of Molecular, Cell, and Developmental Biology, University of California, Los Angeles, Los Angeles, CA 90095, USA
[4]Lead Contact
*Correspondence: nadya.dimitrova@yale.edu
https://doi.org/10.1016/j.molcel.2019.12.014

SUMMARY

The tumor suppressor p53 transcriptionally activates target genes to suppress cellular proliferation during stress. p53 has also been implicated in the repression of the proto-oncogene Myc, but the mechanism has remained unclear. Here, we identify *Pvt1b*, a p53-dependent isoform of the long noncoding RNA (lncRNA) *Pvt1*, expressed 50 kb downstream of *Myc*, which becomes induced by DNA damage or oncogenic signaling and accumulates near its site of transcription. We show that production of the *Pvt1b* RNA is necessary and sufficient to suppress *Myc* transcription in *cis* without altering the chromatin organization of the locus. Inhibition of *Pvt1b* increases *Myc* levels and transcriptional activity and promotes cellular proliferation. Furthermore, *Pvt1b* loss accelerates tumor growth, but not tumor progression, in an autochthonous mouse model of lung cancer. These findings demonstrate that *Pvt1b* acts at the intersection of the p53 and Myc transcriptional networks to reinforce the anti-proliferative activities of p53.

INTRODUCTION

The p53 (also known as TP53) network is a central tumor-suppressive mechanism in mammalian cells that is inactivated in the vast majority of human cancers (Vousden and Prives, 2009). In response to cellular stress induced by DNA damage or oncogenic signaling, p53 transcriptionally activates target genes to limit cellular proliferation or to permanently eliminate damaged cells (Vousden and Prives, 2009). Transcriptional activation by p53 relies on its binding to conserved p53 response elements (p53REs) in the promoters of target genes (Levine and Oren, 2009). p53 has also been implicated in the repression of cell cycle regulators (Engeland, 2018). One of the prominent targets of p53 repression is the Myelocytomatosis (Myc) oncogene (Ho et al., 2005; Levy et al., 1993; Sachdeva et al., 2009), a global transcriptional amplifier that responds to mitogenic signals to promote cellular proliferation (Lin et al., 2012). Multiple models

for how p53 negatively affects *Myc* levels have been proposed, including p53 binding to the *Myc* promoter to suppress histone acetylation, binding to a distal regulatory element to alter nucleosome positioning in the *Myc* promoter, or activating repressive *Myc*-targeting microRNAs (miRNAs) (Ho et al., 2005; Porter et al., 2017; Sachdeva et al., 2009). However, the mechanism of p53-mediated *Myc* downregulation and its contribution to tumor suppression *in vivo* have remained unclear.

Long noncoding RNAs (lncRNAs) can modulate gene expression locally by accumulating near their sites of transcription (Kopp and Mendell, 2018). In dosage compensation, *Xist* and other lncRNAs expressed from the X chromosome specifically repress genes across the entire X chromosome through the recruitment of epigenetic regulators (Lee, 2012). Other *cis*-regulatory lncRNAs act in a more limited, locus-specific manner, such as the p53 target *lincRNA-p21*, proposed to promote the levels of its neighbor *p21* (also known as *Cdkn1a*) by recruiting activating factors (Dimitrova et al., 2014). Although studies of locus-specific *cis*-regulatory lncRNAs have revealed important roles in diverse biological processes (Dimitrova et al., 2014; Elling et al., 2018; Kotzin et al., 2016), characterization of the RNA molecule is often confounded by potential functional roles of DNA regulatory sequences in the lncRNA locus (Bassett et al., 2014; Engreitz et al., 2016; Groff et al., 2016). Defining the RNA-mediated regulation provides important opportunities for RNA-based therapeutics that can alter hardwired molecular interactions to change cellular responses.

Plasmacytoma variant 1 (*Pvt1*), a lncRNA expressed 50 kb downstream of *Myc*, is altered in a large fraction of human cancers. Frequent translocations and viral integrations in the *Pvt1* locus in lymphomas suggest important roles for *Pvt1* in cancer progression (Cory et al., 1985; Graham and Adams, 1986; Graham et al., 1985). In addition, co-amplification of *Myc* and *Pvt1* across multiple cancer types correlates with poor cancer patient prognosis, suggesting cooperation between the two genes during tumorigenesis (Cui et al., 2016; Tseng and Bagchi, 2015; Zeng et al., 2017). This pro-oncogenic cooperation between *Myc* and *Pvt1* was recently confounded by the identification of a p53-binding site in the *Pvt1* locus and by the description of the *Pvt1* promoter as a transcriptional repressor of *Myc* (Cho et al., 2018; Porter et al., 2017). These studies suggested undefined roles for *Pvt1* in cancer progression and a potential crosstalk between the tumor suppressor p53 pathway and the oncogenic Myc network.

doxorubicin, inibitore topoisomerasi2

Tamoxifen is a estrogen receptor modulator
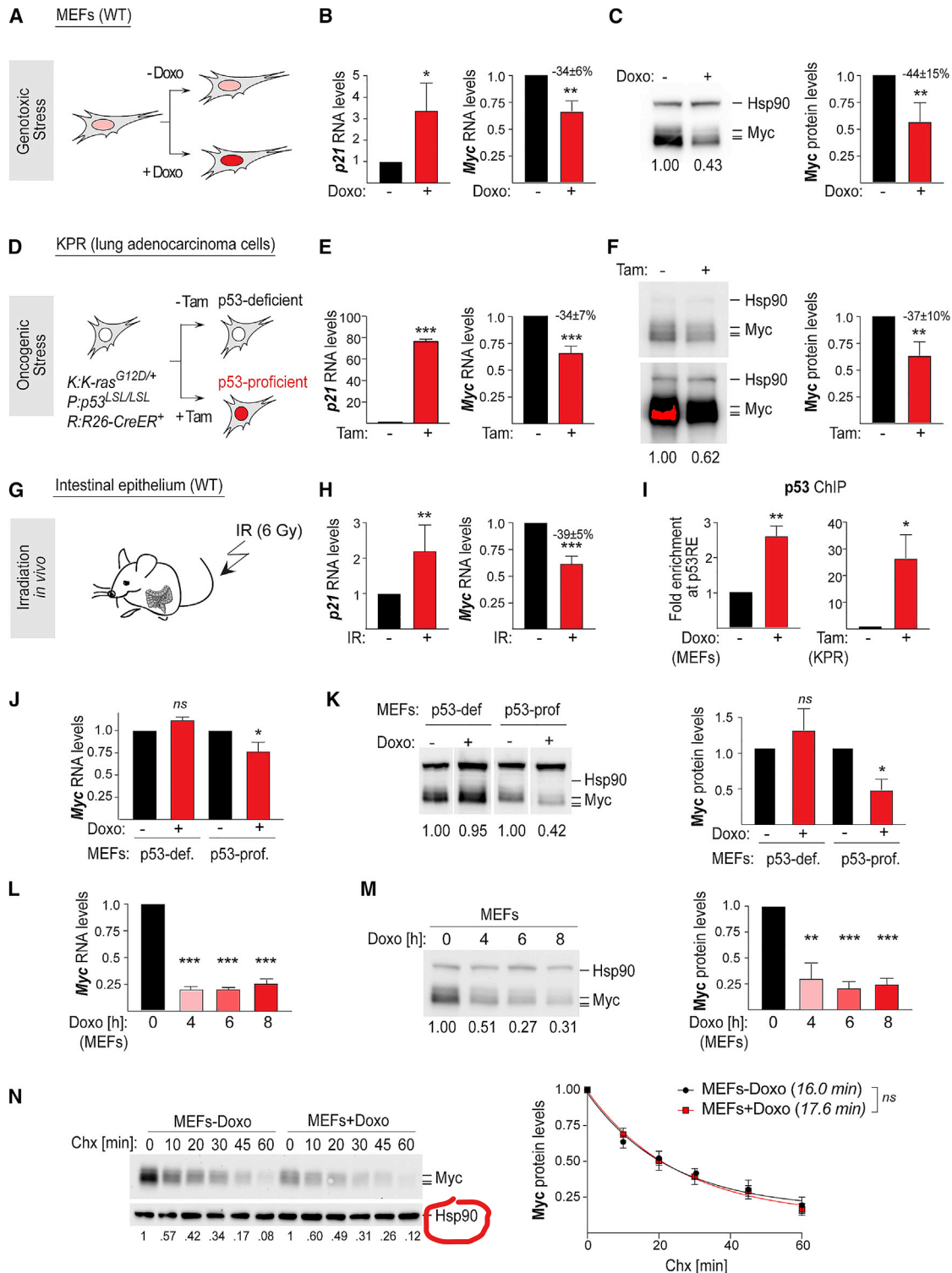
Figure 1. p53 Suppresses *Myc* in Response to Genotoxic and Oncogenic Stress

(A) Schematic of the model system for studying p53-mediated response to genotoxic stress in WT MEFs untreated or treated with Doxo for 24 h. Activation of p53 by passaging or by genotoxic stress is represented by light and dark red nuclei, respectively.

(B) *p21* and *Myc* RNA levels in cells from (A). Data show mean ± SEM (n = 4, biological replicates); *p < 0.05 and **p < 0.01, paired t test.

(C) Left: representative image and quantification of Myc protein levels from cells in (A). Hsp90 as a loading control. Right: bar graph of Myc protein levels showing mean ± SEM (n = 5, biological replicates); **p < 0.01, paired t test.

(legend continued on next page)

In this study, we characterize *Pvt1b*, a p53-induced isoform of the lncRNA *Pvt1*, and we determine its contribution to Myc regulation and the p53 response to stress. We show that production of the *Pvt1b* RNA downstream of p53 represses *Myc* transcription and suppresses cellular proliferation during stress and in the early stages of tumorigenesis. The model presented here illuminates a role for the lncRNA isoform *Pvt1b* as a locus-specific transcriptional regulator that serves to enact selective gene repression downstream of the broad p53 transcriptional activation network.

RESULTS

p53 Suppresses *Myc* under Conditions of Genotoxic and Oncogenic Stress

To gain insight into the mechanism by which p53 causes suppression of *Myc*, we used multiple independent approaches to model the p53-dependent response to stress. To model the cellular response to genotoxic stress, we used wild-type (WT) mouse embryonic fibroblasts (MEFs) treated with the genotoxic agent doxorubicin (Doxo) (Figure 1A). We observed that activation of the p53 transcriptional program following Doxo treatment for 24 h resulted in 3-fold induction of the p53 target *p21* and a concomitant reduction in *Myc* RNA and protein levels by 34% ± 6% (p = 0.008; Figure 1B) and 44% ± 15% (p = 0.0051; Figure 1C), respectively, consistent with previous findings (Ho et al., 2005; Porter et al., 2017). We also found that p53 activation by oncogenic stress, modeled by tamoxifen (Tam)-CreER-dependent restoration of endogenous p53 expression in a murine lung adenocarcinoma cell line (*K-ras*$^{LA2-G12D/+}$; *p53*$^{LSL/LSL}$; *Rosa26-CreER*^{T2}+ [*KPR*]) (Figure 1D) (Feldser et al., 2010), similarly led to a 70-fold activation of *p21*, a 34% ± 7% repression of *Myc* RNA (p = 0.0020; Figure 1E), and a 37% ± 10% decrease in Myc protein (p = 0.0028; Figure 1F). *Myc* repression by 39% ± 5% was also observed in intestinal epithelial cells isolated from mice exposed to 6 Gy of whole-body irradiation, which leads to a well-characterized p53-mediated response to genotoxic stress *in vivo* (p = 0.0007; Figures 1G and 1H) (Clarke et al., 1994). Altogether, these results suggested that *Myc* repression is a general event downstream of p53 transcriptional activation.

In an effort to elucidate the mechanism by which p53 activation results in *Myc* repression, we examined whether p53 associates with the *Myc* locus. We observed that both in Doxo-treated MEFs and Tam-treated *KPR* cells, stress-dependent *Myc* repression was accompanied by binding of p53 to a distal p53RE, located 50 kb downstream of *Myc*, which has previously been implicated in limiting *Myc* expression (Figure 1I)(Porter et al., 2017).

Consistent with p53 dependency, the changes in *Myc* RNA and protein levels were present in p53-proficient, but not p53-deficient, MEFs (Figures 1J and 1K). Additionally, the decrease in *Myc* RNA levels was detectable as early as 4 h following p53 activation and was coincident with the decrease in Myc protein levels, suggesting direct transcriptional modulation by p53 (Figures 1L and 1M). Inhibition of protein translation with cycloheximide (Chx) revealed that Myc protein stability was not significantly affected by the presence of stress, suggesting that the decrease in Myc levels was not due primarily to post-translational regulation (Figure 1N).

Myc Repression Correlates with Activation of a p53-Dependent *Pvt1* Isoform, *Pvt1b*

We were intrigued that the distal p53RE was located within the gene body of the lncRNA *Pvt1* (Figure 2A), which has previously been implicated as a p53 target (Barsotti et al., 2012). Considering lncRNAs can act in *cis* to regulate the transcription of neighboring genes, we examined whether *Pvt1* played a role in restricting *Myc* expression during stress. We noted significant stress-dependent induction of an isoform of *Pvt1*, termed *Pvt1b*, initiated at a transcription start site located immediately downstream of the p53RE. We observed a 3.1 ± 0.2-fold induction of *Pvt1b* in Doxo-treated MEFs (Figure 2B) and a 38 ± 6-fold induction of *Pvt1b* in Tam-treated *KPR* cells (Figure 2C). *Pvt1a*, an isoform of *Pvt1* initiated at exon 1a, was induced to a lesser extent in Doxo-treated MEFs (Figure 2B) and was not significantly induced by Tam in *KPR* cells (Figure 2C). Copy number calculations suggested that *Pvt1b* was induced at 20–210 copies per cell, whereas *Pvt1a* was expressed at 300–400 copies per cell (Figure S1A). Notably, activation of *Pvt1b* was coincident

(D) Schematic of the model system for studying p53-mediated response to oncogenic stress in *KPR* cells untreated or treated with Tam for 24 h. Activation of p53 by oncogenic stress is represented by red nucleus.

(E) *p21* and *Myc* RNA levels in cells from (D). Data show mean ± SEM (n = 6, biological replicates); ***p < 0.001, paired t test.

(F) Left: representative image and quantification of Myc protein levels from cells in (D). Hsp90 as a loading control. Right: bar graph of Myc protein levels showing mean ± SEM (n = 5, biological replicates); **p < 0.01, paired t test.

(G) Schematic of the model system for studying p53-mediated response *in vivo* in intestinal epithelial cells isolated from WT mice at 6 h after 6 Gy whole-body irradiation.

(H) *p21* and *Myc* RNA levels from mice in (G). Data show mean ± SEM (n = 3, biological replicates); **p < 0.01 and ***p < 0.001, unpaired t test.

(I) Enrichment of p53 binding at the *Pvt1*-associated p53RE by ChIP-qPCR in (left) Doxo-treated MEFs and (right) Tam-treated *KPR* cells. Data show mean ± SEM (MEFs, n = 4; *KPR*, n = 3; biological replicates); *p < 0.05 and **p < 0.01, paired t test.

(J) *Myc* RNA levels in p53-deficient or p53-proficient MEFs, untreated or treated with Doxo for 24 h. Data show mean ± SEM (n = 3, biological replicates); ns, not significant; *p < 0.05, paired t test.

(K) Left: representative image and quantification of Myc protein levels from cells in (J). Hsp90 as a loading control. Right: bar graph of Myc protein levels showing mean ± SEM (n = 3, biological replicates); ns, not significant; *p < 0.05, paired t test.

(L) *Myc* RNA levels in WT MEFs, untreated or treated with Doxo for the indicated times. Data show mean ± SEM (n = 4, biological replicates); ***p < 0.001, paired t test.

(M) Left: representative image and quantification of Myc protein levels from cells in (L). Hsp90 as a loading control. Right: bar graph of Myc protein levels showing mean ± SEM (n = 4, biological replicates); **p < 0.01 and ***p < 0.001, paired t test.

(N) Left: representative image and quantification of Myc protein levels following treatment with cycloheximide (Chx) for indicated times in WT MEFs, untreated or treated with Doxo for 8 h. Right: Myc protein half-life (n = 3, biological replicates); ns, not significant, paired t test.
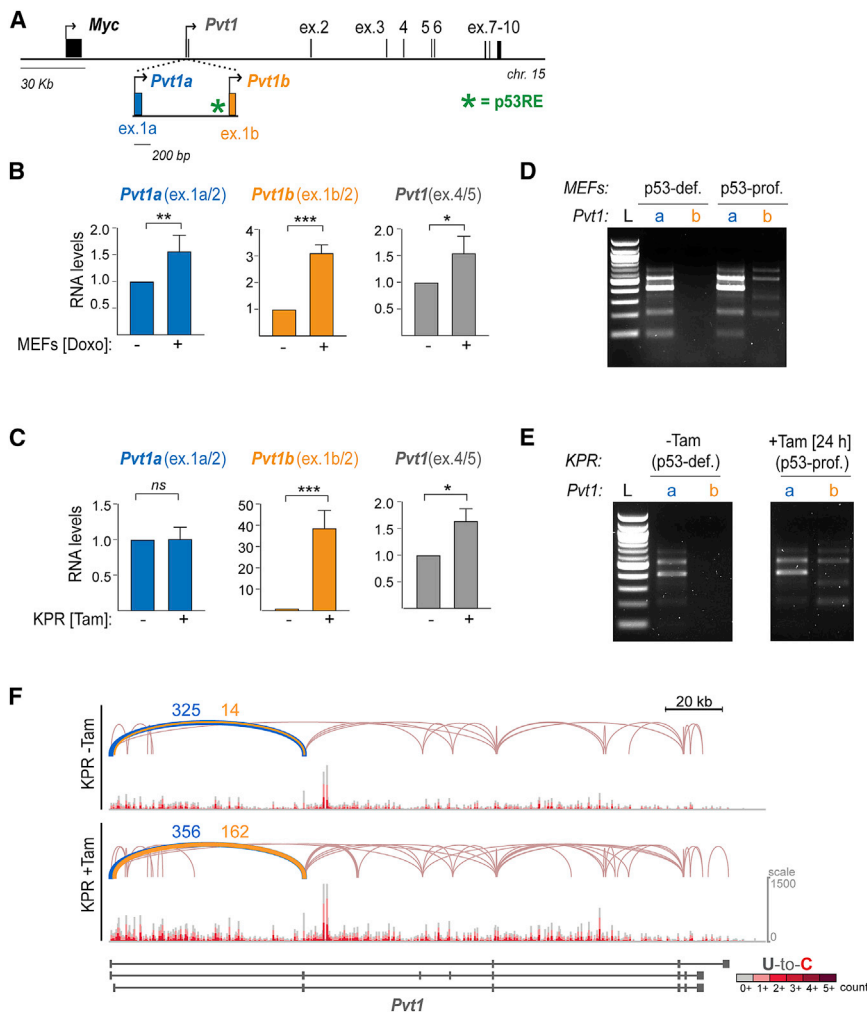
Figure 2. p53-Dependent Induction of the *Pvt1* Isoform *Pvt1b*

(A) Schematic of the mouse *Myc-Pvt1* locus, highlighting exons 1a and 1b of *Pvt1* and the location of the p53RE (green asterisk).

(B and C) Isoform-specific and total *Pvt1* RNA levels detected with primers located in indicated exons in (B) WT MEFs and (C) *KPR* cells, treated as indicated. Data show mean ± SEM (n = 3, biological replicates); *p < 0.05, **p < 0.01, and ***p < 0.001, paired t test.

(D and E) RT-PCR detection of *Pvt1a* isoforms (a, blue), amplified with primers from exon 1a to exon 5, and *Pvt1b* isoforms (b, orange), amplified with primers from exon 1b to exon 5, in RNA isolated from (D) MEFs and (E) *KPR* cells, ladder (L).

(F) Genome browser tracks and Sashimi plots from TimeLapse-seq data in *KPR* cells, treated as indicated. Average number of splice junctions from two biological replicates from exon 1a to exon 2 (blue) and from exon 1b to exon 2 (orange) are indicated.

of the p53-dependent isoform *Pvt1b*, whereas *Pvt1a* represented a largely constitutively expressed isoform.

Stress-Induced *Myc* Repression Occurs in the Absence of Promoter-Enhancer Contact Reorganization

Previous work has shown that CRISPR-mediated transcriptional regulation of the *Pvt1* promoter in p53-deficient cancer cells causes reorganization of the chromatin architecture in the locus and affects the access of *Myc* to downstream enhancers (Cho et al., 2018). To test whether the stress-responsive, p53-dependent induction of *Pvt1b* was associated with changes of these chromatin contacts, we performed chromosome conformation capture (3C) in MEFs and *KPR* cells. Using an anchor in the *Myc* promoter, we confirmed that the *Myc* promoter accessed multiple upstream and downstream enhancers, including previously described *Pvt1* intragenic enhancers (Figures S2A and S2B) (Cho et al., 2018). However, we did not detect significant changes in the chromatin looping between the *Myc* promoter and *Myc*-associated enhancers during the p53-mediated stress response (Figures S2A and S2B). These results argue against a model in which p53-dependent activation of *Pvt1b* leads to reorganization of the three-dimensional architecture of the locus.

Pvt1b Accumulates in the Chromatin Surrounding the *Pvt1-Myc* Locus

To gain insight into the potential regulatory function of *Pvt1b*, we performed single-molecule RNA fluorescence *in situ* hybridization (smRNA-FISH), which allows the visualization of individual RNA molecules by using multiple fluorescently labeled probes per transcript. We designed four independent probe sets to detect *Pvt1* transcripts. *Pvt1a*- and *Pvt1b*-specific probe sets (named *Pvt1a*
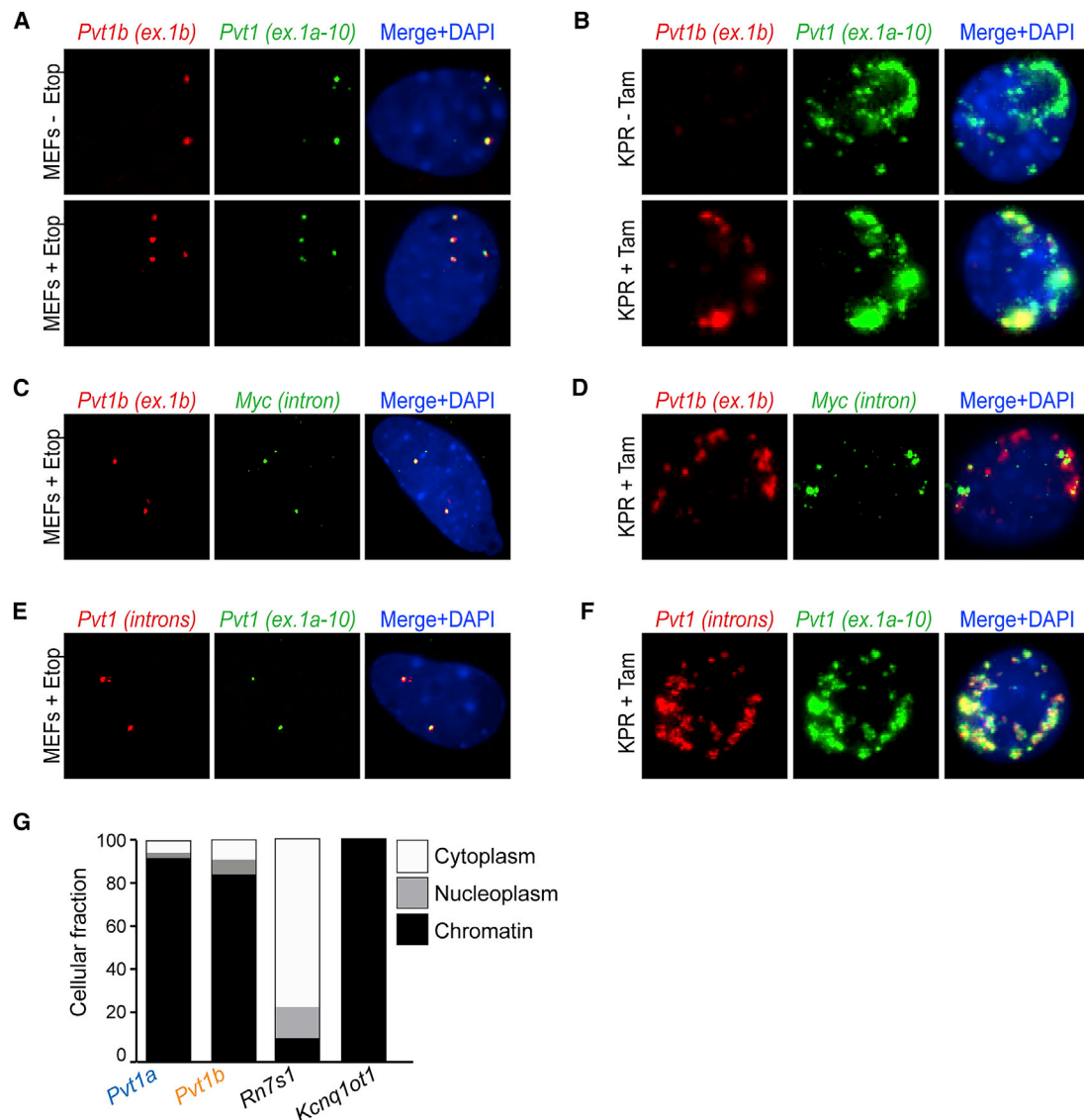
with *Myc* repression and occurred as early as 4 h following Doxo treatment in MEFs (Figure S1B) or 6 h following Tam treatment in *KPR* cells (Figure S1C), consistent with direct transcriptional regulation by p53. Similarly, Doxo-treated human fibroblasts exhibited a 2-fold decrease in *MYC* levels and an 8-fold increase of human *PVT1B* (Figure S1D). These findings indicated that the downregulation of *Myc* and the activation of a p53-dependent, stress-specific *Pvt1* variant are conserved between mouse and human.

To further characterize the transcripts produced from the *Pvt1* locus, we performed RT-PCR with forward primers located in either exon 1a or 1b and a reverse primer in exon 5. We found evidence for extensive alternative splicing and confirmed that variants containing exon 1b were induced by p53, while exon 1a-containing variants were constitutively expressed (Figures 2D and 2E). Despite the splicing heterogeneity, sequencing of nascent RNA revealed that stress-induced *Pvt1b* differed from constitutively expressed *Pvt1a* solely by the use of exon 1b versus exon 1a and exhibited comparable splicing patterns to downstream exons (Figure 2F). We concluded that p53 activation during genotoxic and oncogenic stress initiated transcription in the *Pvt1* locus from exon 1b, leading to the production

Figure 3. Accumulation of *Pvt1* Isoforms in the Chromatin Surrounding the *Pvt1-Myc* Locus
(A–F) smRNA-FISH with indicated probes in (A, C, and E) WT MEFs, untreated or treated with Etop for 24 h and in (B, D, and F) *KPR* cells untreated or treated with Tam for 24 h. DNA, DAPI. Note that *Pvt1b* is detectable in untreated, p53-proficient MEFs, likely because of activation of the p53 pathway by passaging in primary cells, but is undetectable in untreated, p53-deficient *KPR* cells.
(G) *Pvt1a* and *Pvt1b* RNA levels in Doxo-treated WT MEFs following subcellular fractionation (representative from n = 2 biological replicates). *Rn7s1* and *Kcnq1ot1* used as controls for the cytoplasmic and chromatin fractions, respectively.

[*ex.1a*] and *Pvt1b* [*ex.1b*]) were designed against the first exon of each isoform. Although isoform specific, the two probe sets were not expected to detect single RNA molecules, because of the small number of probes per transcript. The probe set *Pvt1 (ex.1a-10)* was designed to detect both full-length *Pvt1a* and full-length *Pvt1b* at single-molecule resolution, whereas the *Pvt1 (introns)* probe set was specific to unspliced Pvt1 molecules. Finally, we designed a probe set to detect *Myc* intronic regions (*Myc* [*intron*]) and mark the site of *Myc* transcription. We observed that *Pvt1a* and *Pvt1b* exhibited a primarily two- or four-dot nuclear pattern in etoposide (Etop)-treated MEFs, reflective of the G1 or S/G2 stages of the cell cycle, respectively (Figures 3A and S3A).

Pvt1a and *Pvt1b* formed larger clouds in Tam-treated *KPR* cells (Figures 3B and S3B), which have amplified the locus, as shown by DNA-FISH (Figure S3C). By co-staining either *Pvt1a* or *Pvt1b* with total *Pvt1*, we concluded that both isoforms exhibited an identical localization pattern (Figures 3A, 3B, S3A, and S3B). Notably, *Pvt1a*- and *Pvt1b*-containing foci co-localized with signals specific to the introns of nascent *Myc* (Figures 3C and 3D) as well as with nascent *Pvt1* transcripts (Figures 3E and 3F). These results led us to conclude that following transcription, *Pvt1a* and *Pvt1b* are retained on the chromatin surrounding the *Pvt1-Myc* locus. Subcellular fractionation analysis confirmed enrichment of both *Pvt1* variants in the chromatin fraction (Figure 3G).
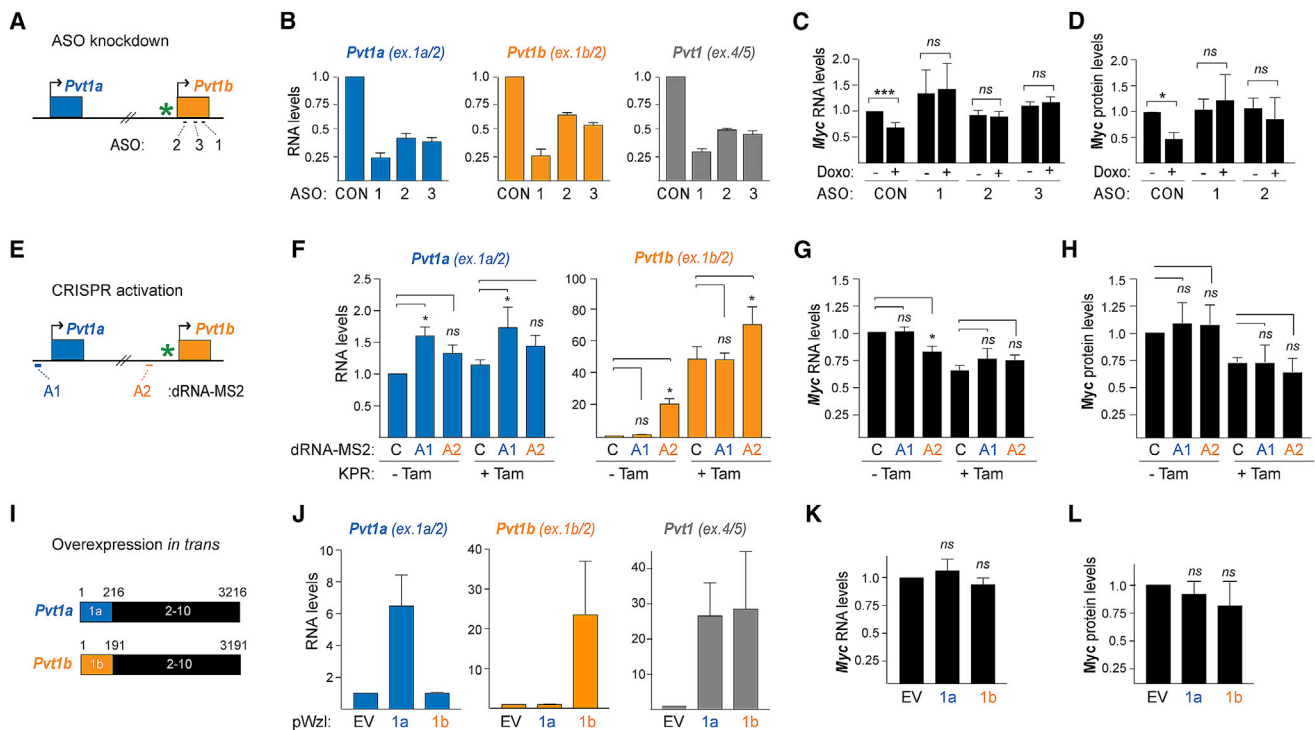
Figure 4. Production of *Pvt1b* RNA Suppresses *Myc* Expression In *cis*

(A) Schematic of ASO design. Asterisk denotes p53RE.

(B) Isoform-specific and total *Pvt1* RNA levels in WT MEFs transfected with indicated control (CON) or *Pvt1*-targeting ASOs and harvested 24 h post-Doxo treatment. Data are normalized to CON and show mean ± SEM (n = 3, biological replicates).

(C) *Myc* RNA levels in cells from (B), untreated or treated with Doxo for 24 h. Data are normalized to CON-Doxo and show mean ± SEM (n = 3, biological replicates); ns, not significant; ***p < 0.001, paired t test.

(D) Quantification of Myc protein levels in cells from (B). Data are normalized to CON-Doxo and show mean ± SEM (n = 3, biological replicates); ns, not significant; *p < 0.05, paired t test.

(E) Schematic of CRISPRa dRNA design. Asterisk denotes p53RE.

(F) *Pvt1a* and *Pvt1b* RNA levels following *Pvt1a* (A1) or *Pvt1b* (A2) transcriptional activation in *KPR* cells, untreated or treated with Tam for 24 h. Data are normalized to control dRNA (C) and show mean ± SEM (n = 5, biological replicates); ns, not significant; *p < 0.05, paired t test.

(G) *Myc*-RNA levels from experiment in (F); ns, not significant; *p < 0.05, paired t test.

(H) Quantification of Myc protein levels in cells from (F). Data show mean ± SEM (n = 3, biological replicates); ns, not significant, paired t test.

(I) Schematic of *Pvt1a* and *Pvt1b* overexpression constructs.

(J) Isoform-specific and total *Pvt1* RNA levels in WT MEFs transiently overexpressing full-length *Pvt1a* (1a) or *Pvt1b* (1b). Data are normalized to empty vector (EV) and show mean ± SEM (n = 3, biological replicates); ns, not significant, paired t test.

(K) *Myc* RNA levels from experiment in (J).

(L) Quantification of Myc protein levels in cells from (J). Data show mean ± SEM (n = 3, biological replicates); ns, not significant, paired t test.

Pvt1b RNA Represses *Myc* Levels In *cis*

On the basis of the stress-dependent expression of *Pvt1b* and its local chromatin accumulation, we hypothesized that *Pvt1b* could be involved in *Myc* repression through an RNA-dependent mechanism. To directly test this hypothesis, we designed three independent antisense oligonucleotides (ASOs) specific to exon 1b (Figure 4A). We used a non-targeting ASO (CON) as a negative control. As ASOs lead to co-transcriptional RNA cleavage and degradation, ASO1, ASO2, and ASO3 significantly downregulated both *Pvt1a* and *Pvt1b* (Figure 4B).

Next, we examined how *Pvt1*-targeting ASOs affected *Myc* expression levels. In untreated MEFs, *Myc* RNA and protein levels were not significantly altered in ASO compared with CON samples, indicating that knockdown of *Pvt1* isoforms did not affect *Myc* regulation in the absence of stress, consistent with

previous findings (Figures 4C, 4D, and S4A) (Cho et al., 2018). As expected, upon treatment with Doxo, CON MEFs experienced a significant decrease in *Myc* RNA (Figure 4C) and protein levels (Figures 4D and S4A). On the other hand, we found that *Pvt1*-targeting ASOs completely rescued stress-induced downregulation of *Myc* RNA and protein (Figures 4C, 4D, and S4A). These findings revealed that transcriptional activation of *Pvt1b* by p53 is required for *Myc* repression during stress. As a control, the absence of *Myc* downregulation was not due to altered association of p53 with the *Pvt1b*-associated p53RE (Figure S4B).

To test the sufficiency of *Pvt1b* in suppressing *Myc*, we used the CRISPR-SAM (synergistic activation mediator) system to activate the expression of endogenous *Pvt1b* in p53-deficient cells (Dahlman et al., 2015). CRISPR-SAM combines nuclease-proficient Cas9 with 15-nucleotide "dead

RNAs'' (dRNAs), which are competent for Cas9 recruitment but do not support Cas9 nuclease activity. In CRISPR-SAM, the dRNA scaffold is extended by two MS2-binding loops (dRNA-MS2), which serve to recruit the MS2-binding protein (MBP) fused to the transcriptional activator domains of p65 and HSF1, allowing CRISPR activation (CRISPRa) of target genes (Dahlman et al., 2015). We designed A1 and A2 dRNA-MS2 targeting the promoters of *Pvt1a* and *Pvt1b*, respectively (Figure 4E). Compared with a non-targeting control (C), CRISPRa using A1 led to 1.6-fold induction of *Pvt1a*, without altering *Pvt1b* levels, whereas A2 resulted in a 20-fold activation of *Pvt1b* with no significant induction of *Pvt1a* (Figure 4F). Next, we examined the effect of activation of endogenous *Pvt1a* and *Pvt1b* on *Myc* levels. In support of our model, we found that CRISPRa of *Pvt1b*, but not *Pvt1a*, was sufficient to significantly repress *Myc* RNA in p53-deficient cells compared with control dRNA-expressing cells (p = 0.023; Figure 4G). Activation of *Pvt1b* did not further downregulate *Myc* levels following p53 restoration, indicating that *Pvt1b* acted downstream of p53 (Figure 4G). On the other hand, activation of *Pvt1b* was not sufficient to suppress Myc protein levels, opening the possibility for *Pvt1b*-independent input at the post-transcriptional level (Figures S4C and 4H).

To distinguish between activity in *cis* versus in *trans*, we tested whether exogenous overexpression of *Pvt1a* and *Pvt1b* by transfection of cDNA constructs containing exons 1a-10 (1a) or 1b-10 (1b) affected Myc expression (Figure 4I). We observed a 6.5-fold overexpression of *Pvt1a* as well as a 23-fold overexpression of *Pvt1b*, which were comparable with CRISPRa-induced overexpression (Figure 4J). However, we found that exogenously delivered *Pvt1a* or *Pvt1b* did not significantly affect *Myc* RNA or protein levels, arguing against an effect in *trans* (Figures 4K, 4L, and S4D). Altogether, these data supported a previously unappreciated role for *Pvt1b*, but not *Pvt1a*, in the repression of *Myc* in *cis*.

Genetic Inhibition of *Pvt1b* Reverses Stress-Induced *Myc* Downregulation

To investigate the functional contribution of *Pvt1b* to the p53 tumor-suppressor pathway, we developed a genetic approach to specifically inhibit *Pvt1b* expression by mutating the p53RE required for its expression. We targeted Cas9 to the *Pvt1b* p53RE by designing a guide RNA (gRNA; ΔRE) adjacent to the GGG protospacer-adjacent motif (PAM) site located in the central region of the p53 consensus binding motif (Figure 5A). A non-targeting gRNA (Con) was used as a negative control. We generated control (Con) and mutant (ΔRE) *KPR* population, MEF population, and *KPR* clonal cell lines, which contain numerous or clone-specific CRISPR/Cas9-induced mutations of the *Pvt1b*-associated p53RE. We confirmed mutagenesis of the p53RE by Sanger sequencing (Figures 5A, S5A, and S5B) and showed by chromatin immunoprecipitation (ChIP) that ΔRE mutagenesis reduced p53 binding by 15-fold (Figure 5B). Importantly, by qRT-PCR, *Pvt1b* levels were significantly suppressed in ΔRE cells compared with controls (Figures 5C, S5C, S5D, and S5G), and by smRNA-FISH, we observed loss of *Pvt1b*-specific signal in Tam-treated ΔRE *KPR* cells compared with Tam-treated controls (Figures 5D and 5E). These observations led us to conclude that mutagenesis of the *Pvt1b*-associated p53RE resulted in efficient abrogation of stress-dependent *Pvt1b* activation.

Next, we queried whether ΔRE mutagenesis led to isoform-specific inhibition. By qRT-PCR and smRNA-FISH, we found that *Pvt1a* RNA levels and localization pattern were not significantly altered in ΔRE *KPR* population and clonal cell lines compared with controls, indicating that mutation of the p53RE led to specific inhibition of *Pvt1b* in *KPR* cells (Figures 5C, 5D, S5C, and S5D). On the other hand, mutagenesis of the p53RE in MEFs led to a significant reduction of *Pvt1a* (Figure S5G), consistent with our findings that *Pvt1a* expression has a p53-dependent component in this cell type (Figure 2B).

Finally, we examined by qRT-PCR and immunoblotting the effects of the ΔRE mutation and the resulting loss of *Pvt1b* expression on *Myc* levels during the cellular response to stress. In Con *KPR* population, *KPR* clonal, and MEF lines, exposure to oncogenic or genotoxic stress led to the expected significant decrease in *Myc* RNA (Figures 5F, S5E, S5F, and S5H) and protein levels (Figures 5G, 5H, S5I, and S5J). In contrast, exposure to stress in ΔRE *KPR* population, *KPR* clonal, and MEF lines did not lead to a significant decrease in *Myc* RNA levels compared with unstressed cells, consistent with the ASO data (Figures 5F, S5E, S5F, and S5H). These results provided an independent, genetic confirmation that *Pvt1b* regulates *Myc* RNA levels downstream of p53.

Interestingly, although Myc protein levels were significantly elevated in ΔRE *KPR*+Tam and ΔRE MEF+Doxo lines compared with Con *KPR*+Tam and Con MEF+Doxo lines, respectively, the rescue was not complete (Figures 5G, 5H, S5I, and S5J), consistent with the possibility of *Pvt1b*-independent regulatory input at the post-transcriptional level (Figure 4H).

Of note, mutagenesis of the *Pvt1b*-associated p53RE did not affect the long-range chromatin interactions in the locus, consistent with chromatin architecture not playing a significant role in p53-mediated Myc repression (Figure S6A).

Pvt1b Suppresses Myc Transcriptional Activity and Cellular Proliferation *In Vitro*

By analyzing the effects of the ΔRE mutation on gene expression in total RNA from untreated and Doxo-treated ΔRE and Con MEFs, we confirmed that *Myc* is a target of *Pvt1b* regulation in response to stress (Figure 6A). Next, to test whether *Pvt1b* acted at the transcriptional or post-transcriptional level, we sequenced nascent RNA from untreated and Tam-treated ΔRE and Con *KPR* cells (Schofield et al., 2018). We found that nascent *Myc* transcripts were significantly upregulated in ΔRE+Tam compared with Con+Tam *KPR* cells, indicative of transcriptional regulation (Figures 6B and 6C). These data revealed that *Pvt1b* production promotes transcriptional suppression of *Myc*.

Next, we queried how the changes in *Myc* RNA levels affected the Myc transcriptional program by examining the consequence of *Pvt1b* loss on a curated set of 196 Myc target genes (gene set enrichment analysis, HALLMARK_MYC_TARGETS_V1; Liberzon et al., 2015). We plotted the cumulative frequency distribution of the fold change (FC) of Myc target genes in ΔRE cells relative to Con cells in the presence of stress (log FC [ΔRE/Con+stress]). Compared with a randomly generated set of control genes expressed at comparable levels, we found a
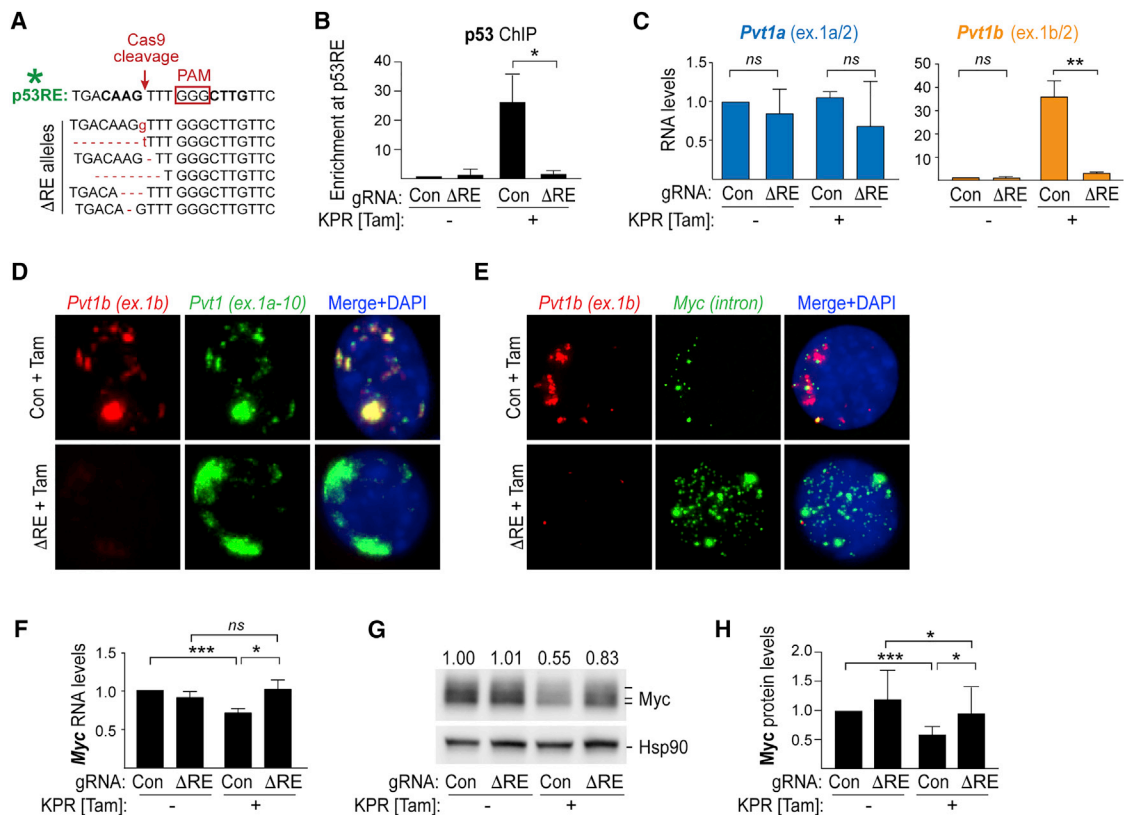
Figure 5. Genetic Inhibition of *Pvt1b* Leads to Increased *Myc* Levels

(A) Top: schematic of p53RE mutagenesis, indicating the PAM site (red box) and Cas9 cleavage site (red arrow). Bottom: mutant alleles, determined by Sanger sequencing.

(B) ChIP-qPCR analysis of p53 enrichment at *Pvt1b*-associated p53RE in indicated cells and treatments. Data show mean ± SEM (n = 3, biological replicates); *p < 0.05, paired t test.

(C) *Pvt1a* and *Pvt1b* RNA levels in indicated cells and treatments. Data show mean ± SEM (n = 3, biological replicates); ns, not significant; **p < 0.01, paired t test.

(D and E) smRNA-FISH of *Pvt1b* (ex.1b, red) co-localized with (D) total *Pvt1* (ex1a-10, green) or (E) nascent *Myc* (intron, green) in indicated cells and treatments. DNA, DAPI.

(F) *Myc* RNA levels in indicated cells and treatments. Data show mean ± SEM (n = 3, biological replicates); ns, not significant; *p < 0.05 and ***p < 0.001, paired t test.

(G) Representative image and quantification of Myc protein levels in indicated cells and treatments. Hsp90 as a loading control.

(H) Quantification of Myc protein levels from experiments in (G). Data show mean ± SEM (n = 6, biological replicates); *p < 0.05 and ***p < 0.001, paired t test.

significant increase in the levels of Myc targets in MEFs and *KPR* cells (Figures 6D and 6E). We concluded that *Myc* derepression by ΔRE mutagenesis led to a small but significant increase in the transcriptional activity of Myc.

Considering that Myc target genes include factors that promote cellular growth, we compared the proliferation of mutant cells with controls. It has previously been shown that Tam-mediated p53 restoration in *KPR* cells leads to a permanent cell-cycle arrest called senescence (Feldser et al., 2010). Although loss of *Pvt1b* expression did not overcome senescence, it led to a significant increase in cellular proliferation and colony formation compared with control cells (Figures 6F and 6G). As a control, the ΔRE mutation did not affect *Myc* levels and proliferation in p53-deficient cells, ruling out off-target effects (Figures S6B and 6F). These data suggested that *Pvt1b* mediates specific aspects of p53 function to suppress the proliferative potential of cells *in vitro*.

Tumor-Specific Inhibition of *Pvt1b* Promotes Tumor Growth *In Vivo*

Inactivation of p53 in the *K-ras*[LSL-G12D/+](*K*) autochthonous mouse model of lung cancer has been shown to increase tumor burden and promote tumor progression from benign to aggressive disease (DuPage et al., 2009; Jackson et al., 2001, 2005). To elucidate whether *Pvt1b* mediated some aspects of p53 function *in vivo*, we performed tumor-specific mutagenesis of the *Pvt1b*-associated p53RE (Figure 7A). We built a bifunctional lentiviral construct (*U6-gRNA PGK-Cre* [*UGPC*]) for co-expression of the ΔRE gRNA (UGPC-ΔRE) and Cre recombinase, required for Cas9 targeting and tumor initiation, respectively (DuPage et al., 2009). Expression of Cas9 in a tumor-specific manner was achieved by crossing the *K* model to *Rosa26-Cas9*[LSL] (*C*) mice to generate *KC* animals (Platt et al., 2014). As a negative control, we used a non-targeting control (UGPC-Con). As a positive control, we used a previously described gRNA that targets
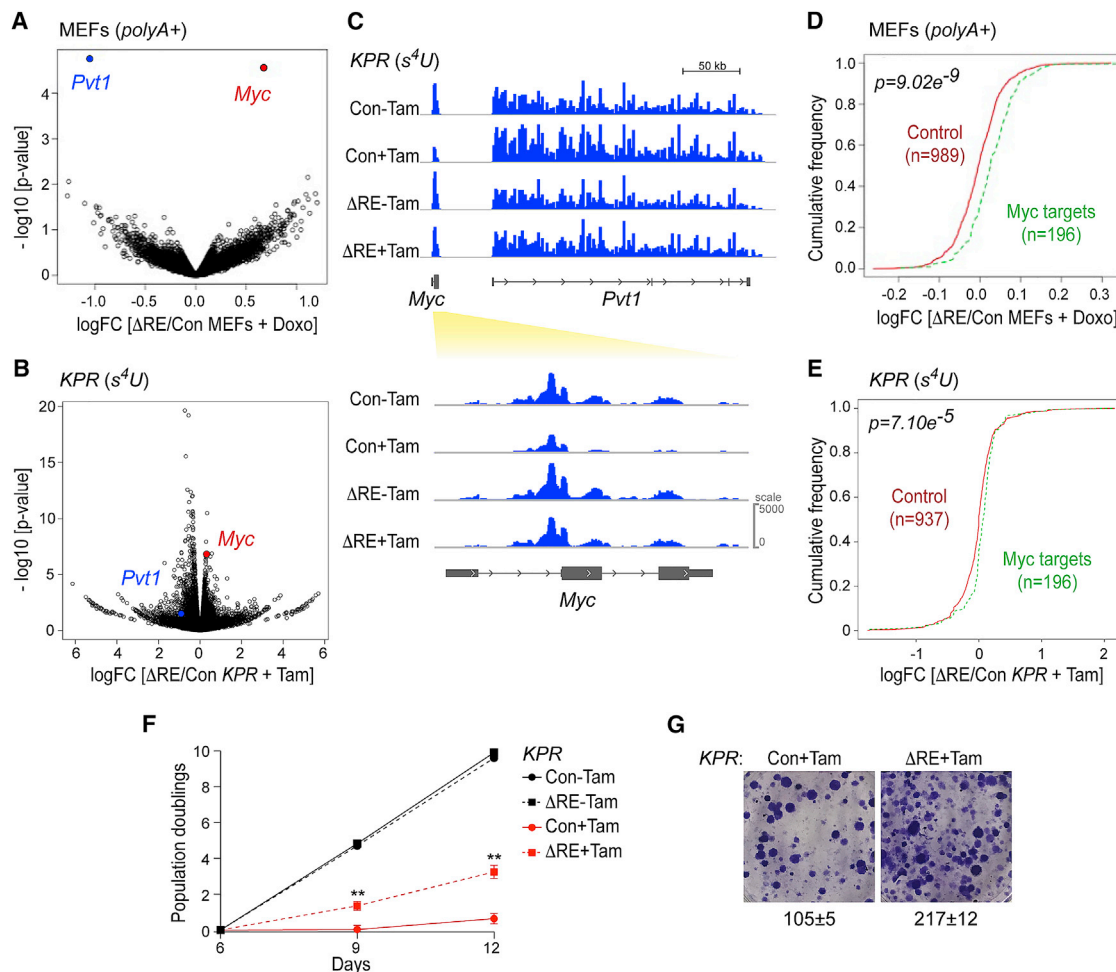
Figure 6. *Pvt1b* Suppresses *Myc* Transcription and Proliferative Function

(A and B) Butterfly plot depicting the fold change (log FC) in gene expression of indicated samples relative to statistical significance ($-\log_{10}$[p value]; MEF, n = 3; *KPR*, n = 2; biological replicates). Gene expression profiling was performed by (A) RNA-seq of polyA-selected RNA isolated from Con or ΔRE gRNA-expressing MEFs, untreated or treated with Doxo for 24 h, or (B) TimeLapse-seq of ribosomal cDNA-depleted s^4U-labeled RNA isolated from Con or ΔRE gRNA-expressing *KPR* cells, untreated or treated with Tam for 16 h. Total *Pvt1* (blue) and *Myc* (red) are labeled.

(C) Top: Genome Browser tracks depicting the *Myc-Pvt1* locus from transient-transcriptome (TT) Time-Lapse-seq. Bottom: detail of the *Myc* locus.

(D and E) Cumulative frequency distribution plot of differential expression for a set of curated Myc target genes and a matched set of control genes from analyses in (A) and (B).

(F) Population doublings in Con or ΔRE gRNA-expressing *KPR* cells, untreated or treated with Tam over indicated time course. Data show mean ± SEM (n = 3, biological replicates); **p < 0.01, unpaired t test.

(G) Representative images of colony formation assay of Tam-treated *KPR* cells, infected with Con or ΔRE gRNAs. Numbers show mean ± SEM (n = 3, biological replicates); **p < 0.01, unpaired t test.

the open reading frame of p53 (UGPC-p53KO) (Xue et al., 2014). Sanger sequencing confirmed successful mutagenesis of the *Pvt1b*-associated p53RE in UGPC-ΔRE-infected animals (Figure 7B).

We next examined hematoxylin and eosin (H&E) sections of lungs from mice infected with UGPC-Con, UGPC-p53KO, and UGPC-ΔRE virus and sacrificed at 16 weeks post-tumor initiation. In the K model, progression of atypical adenomatous hyperplasia (AAH; grade 1) and lung adenoma (grade 2) to adenocarcinoma (grade 3) and invasive adenocarcinoma (grade 4) is promoted by loss of p53 function (Jackson et al., 2005). Indeed, histopathological analysis revealed that all of the tumors

(53 of 53) in UGPC-Con-infected animals manifested grade 1 features (Figures 7C and 7D). In contrast, 70% of UGPC-p53KO-expressing tumors (39 of 56) were marked by atypical nuclei, desmoplasia, and transition to a poorly differentiated phenotype and were classified as grade 2 or 3 (Figures 7C and 7D) (DuPage et al., 2009). On the basis of these data, we estimated that a large portion of the tumors underwent successful CRISPR/Cas9 editing *in vivo*. Editing of the *Pvt1b*-associated p53RE resulted in tumors with histopathological features comparable with controls, and only 3% of tumors (2 of 67) in UGPC-ΔRE-infected animals were classified grade 2 or 3, suggesting that tumor progression was not accelerated by *Pvt1b* inhibition (Figures 7C and 7D). We
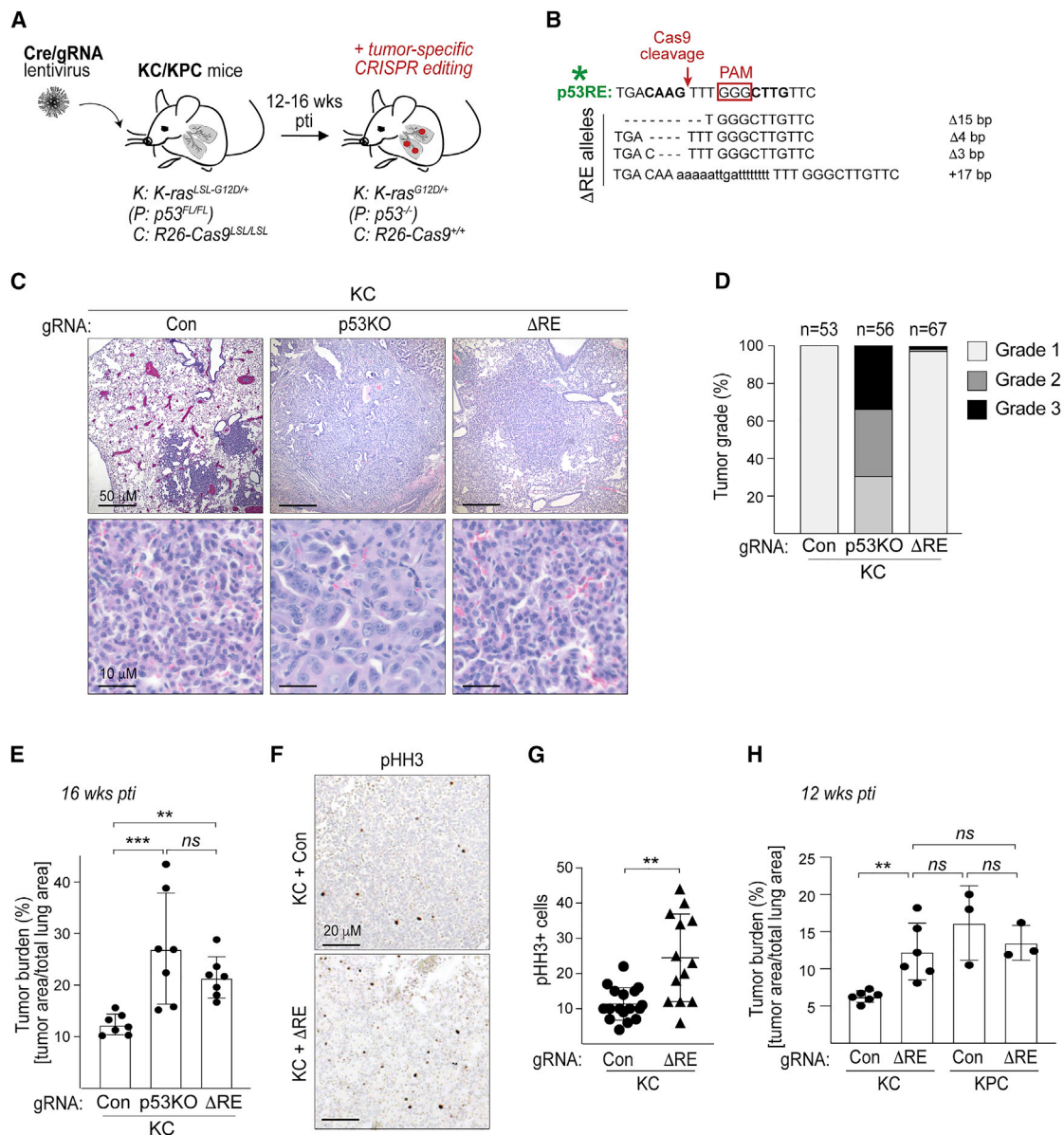
Figure 7. Tumor-Specific Editing in a Lung Cancer Model Reveals a Role for *Pvt1b* in Suppressing Tumor Growth, but Not Progression

(A) Schematic of tumor-specific gene editing in *KC* and *KPC* lung cancer mouse models.

(B) Mutant ΔRE alleles, determined by Sanger sequencing of bulk DNA isolated from tumor-bearing lungs.

(C) H&E staining of lung sections of *KC* mice infected with indicated gRNAs and analyzed at 16 weeks post-tumor initiation (pti). Scale bars as indicated.

(D) Quantification of tumor grade in mice described in (C). The number of tumors analyzed from n = 5 mice is indicated for each group.

(E) Quantification of tumor burden in mice described in (C). Dots represent individual animals and bar graph shows mean ± SEM (n = 7 mice); ns, not significant; **p < 0.01 and ***p < 0.001, unpaired t test.

(F) Representative images of immunohistochemistry for the mitotic marker pHH3 in lung sections from (C). Scale bars as indicated.

(G) Quantification of images in (F). Data show mean ± SEM of n = 13–17 tumors from n = 5 mice; **p < 0.01, Mann-Whitney test.

(H) Quantification of tumor burden in *KC* and *KPC* mice infected with indicated gRNAs and analyzed at 12 weeks pti. Dots represent individual animals, and bar graph shows mean ± SEM (KC, n = 6 mice; KPC, n = 3 mice); ns, not significant; *p < 0.05, unpaired t test.

concluded that *Pvt1b* does not likely mediate the ability of p53 to restrain tumor progression from benign hyperplasia to advanced disease.

On the other hand, quantification of the tumor area relative to the total lung area revealed that the tumor burden in UGPC-ΔRE-infected animals (21% ± 4%) was significantly increased compared with the burden of control mice (12% ± 2%) (p = 0.0040; Figure 7E). Notably, the tumor burden in p53RE-edited mice was comparable with the tumor burden in UGPC-p53KO-infected mice (26% ± 3%) (Figure 7E). These findings suggested

that *Pvt1b* mediated in large part the growth-restrictive functions downstream of p53, particularly during the pre-malignant stages of the disease. As a control for potential off-target effects of Cas9 expression and CRISPR editing, we used two independent single guide RNAs (sgRNAs) (sg1 and sg2) to target the p53RE in intron 1 of an unrelated lncRNA, *Gm26542*, for which we had evidence for direct p53 regulation (Figures S7A–S7C). In contrast to *Pvt1b*, inhibition of *Gm26542* did not affect proliferation in Tam-treated *KPR* cells *in vitro* (Figure S7D) and did not significantly alter the tumor burden in *KC* mice *in vivo* (Figure S7E).

The increase in tumor burden in UGPC-ΔRE-infected animals compared with UGPC-Con mice was not due to decreased apoptosis, as there was no evidence for cleaved caspase-3 (CC3) immunohistochemistry (IHC) staining in lung sections. Instead, the increase in tumor burden could be attributed to enhanced proliferation, as manifested by the significantly greater number of phosphorylated histone H3 (pHH3)-positive mitotic cells in *Pvt1b*-deficient tumors from UGPC-ΔRE-infected animals compared with tumors from UGPC-Con-infected mice (p = 0.0026; Figures 7F and 7G).

Finally, to investigate whether *Pvt1b* acted downstream or independent of p53, we performed an epistasis experiment. We generated cohorts of either *KC* or *K-ras*$^{LSL-G12D/+}$; *p53*$^{FL/FL}$; *Rosa26-Cas9*$^{LSL/LSL}$ (*KPC*) animals, which have genetically engineered Cre-inducible loss-of-function alleles of p53. We analyzed tumor burden at 12 weeks post-tumor initiation with UGPC-Con or UGPC-ΔRE virus. Consistent with our findings above, we observed a significant increase in the tumor burden of UGPC-ΔRE-infected mice compared with UGPC-Con-infected *KC* animals (p = 0.0035; Figure 7H). In contrast, we found that the tumor burden was not significantly different between UGPC-ΔRE and UGPC-Con-infected *KPC* animals (Figure 7H). Moreover, there was no statistically significant difference between the tumor burden of *KC* mice infected with UGPC-ΔRE and *KPC* mice infected with UGPC-Con (Figure 7H). Altogether, these results revealed that *Pvt1b* and p53 enhance the expansion of pre-malignant tumors through a common pathway.

DISCUSSION

Our study provides new mechanistic insights into the function of the lncRNA *Pvt1* in the context of the p53 tumor suppressor pathway. We identify a conserved isoform of *Pvt1*, *Pvt1b*, that is directly activated by p53 in response to genotoxic and oncogenic stress. Our data reveal that production of *Pvt1b* functions as a p53-dependent mechanism that is wired into the *Myc-Pvt1* locus to directly and swiftly downregulate *Myc* transcription during stress. This appears to be the primary mechanism underlying stress-induced Myc reduction at the transcriptional level, although our data are also consistent with *Pvt1b*-independent regulation at the post-transcriptional level.

Functionally, we observed that *Pvt1b* activation leads to restricted Myc levels and transcriptional activity and suppressed cellular proliferation. Furthermore, using an autochthonous mouse model of lung cancer, we determined that *Pvt1b* acts downstream of p53 during the early stages of cancer development to limit tumor growth. Strikingly, in this respect, epistasis analysis suggested that *Pvt1b* acts as the primary mediator of

p53. On the other hand, we found that *Pvt1b* is not involved in other aspects of p53 function, such as promoting senescence or limiting tumor progression to advanced disease. Altogether, these analyses define the specific contributions of *Pvt1b* downstream of p53, pointing to growth-limiting and tumor-suppressive functions of *Pvt1b* in the context of cancer. These conclusions contrast the common classification of *Pvt1* as an oncogene, which is based on extensive correlative evidence linking *Pvt1* aberrations with increased invasive capacities of cancer cells and poor patient survival (Guan et al., 2007; Guo et al., 2018; Kong et al., 2015; Riquelme et al., 2014; Tseng et al., 2014; Zeng et al., 2017; Zhang et al., 2019; Zhao et al., 2018; Zheng et al., 2016; Zhu et al., 2017). On the other hand, our data are consistent with recent reports of tumor-suppressive elements in the *Pvt1* locus (Barsotti et al., 2012; Cho et al., 2018; Porter et al., 2017).

Our findings shed light on a subset of genomic aberrations reported across a variety of malignancies, which represent translocations between the first exon of *Pvt1a* fused to various 3′ gene partners (Iwakawa et al., 2013; Kim et al., 2014; Nagoshi et al., 2012; Northcott et al., 2012). Such rearrangements would be expected to separate the *Myc* locus from *Pvt1b*, providing cells with a proliferative advantage due to the inability of p53 to suppress *Myc* levels during early stages of tumor development. On the other hand, the proposed tumor-suppressive role of *Pvt1b* is at odds with the common amplification of the *Pvt1* locus in cancer (Guan et al., 2007; Riquelme et al., 2014). We propose that amplification of other elements, such as the *Pvt1a* transcript or *Pvt1*-associated *Myc* enhancers may be the drivers of oncogenic activities in this setting, as proposed by others (Tseng et al., 2014; Cho et al., 2018). Alternatively, these alterations might be occurring following p53 inactivation, which would preclude *Pvt1b* expression.

Mechanistically, we provide direct evidence for a role of *Pvt1b* RNA production in *Myc* regulation. Antisense-mediated depletion experiments reveal that *Pvt1b* is required for stress-induced *Myc* inhibition, whereas epigenetic activation from the endogenous locus shows that *Pvt1b* is sufficient to repress *Myc* in the absence of stress or a functional p53 pathway. Although ASO-based knockdown and CRISPR-guided epigenetic experiments cannot formally differentiate between the mature *Pvt1b* molecules or the production of nascent *Pvt1b* transcripts as the mediator of *Myc* repression, our data support an RNA-based mechanism.

This conclusion differs from the recent finding that the *Pvt1a* promoter suppresses *Myc* levels in an RNA-independent manner (Cho et al., 2018). The discrepancy can potentially be explained by the previous focus on the constitutive *Pvt1* isoform, by the use of p53-deficient cell lines, or by the use of ineffective ASOs (Cho et al., 2018). Alternatively, we propose that the two tumor-suppressive activities in the *Pvt1* locus, one p53 and RNA dependent and the other p53 and RNA independent, may co-exist and operate in distinct cellular contexts. Our findings also do not contradict studies that have implicated *Pvt1a* or circular *Pvt1* isoforms as oncogenes via diverse mechanisms, such as oncoprotein stabilization or competition for miRNA binding (Tseng et al., 2014; Xu et al., 2017; Zhao et al., 2018). Indeed, the complexity of the *Pvt1* locus highlights the need for further rigorous dissection of the various alternative start site and splice variants.

It is important to note that *Pvt1b* mediates a repressive event downstream of p53, which is a well-characterized transcriptional activator. Considered in the context of the previously characterized p53-dependent *cis*-regulatory *lincRNA-p21* (Dimitrova et al., 2014), it appears that transcription factors use lncRNAs to either enhance their inherent activity or to allow reverse regulation within local circuits. LncRNAs that accumulate at their sites of transcription, such as *Pvt1b*, are poised to act as modulators of gene expression in a locus-specific manner. Indeed, *Pvt1b* activation leads to *Myc* repression within 4 h of exposure to genotoxic stress, which is comparable with the kinetics of activation of p53 target genes. We propose that production and/or chromatin accumulation of p53-induced *Pvt1b* transcripts acts in *cis* during the cellular response to stress to rapidly influence the transcriptional environment at the *Myc* promoter. Thus, locus-specific transcriptional regulation by lncRNAs may provide additional tools within a transcription program that allow dynamic and swift responses to cellular challenges. As the mechanisms of more p53-dependent lncRNAs are revealed, we can gain new insight into how regulatory RNAs contribute to the cellular responses to stress mediated by p53. Although future work will determine the functional elements of *Pvt1b* transcripts, the widespread importance of this regulatory circuit in normal and transformed cells *in vitro* and *in vivo* suggests the possibility of controlling *Myc* levels in cancer by modulating *Pvt1b* activity.

STAR★METHODS

Detailed methods are provided in the online version of this paper and include the following:

- KEY RESOURCES TABLE
- LEAD CONTACT AND MATERIALS AVAILABILITY
- EXPERIMENTAL MODEL AND SUBJECT DETAILS
  - Mouse strains
  - Cell culture and drug treatments
  - Constructs
- METHOD DETAILS
  - RNA isolation and qRT-PCR
  - Immunoblotting
  - Chromatin immunoprecipitation (ChIP)
  - Single-molecule FISH (smRNA-FISH)
  - DNA-Fluorescence *in situ* hybridization (FISH)
  - Subcellular fractionation
  - Antisense knockdown
  - Chromosome Conformation Capture (3C)
  - RNA-seq
  - Transcriptome-wide TimeLapse-seq
  - TT-TimeLapse-seq
  - TimeLapse-seq mutational analysis
  - Differential expression analysis
  - Growth curve and colony assay
  - Tumor studies
  - Immunohistochemistry
- QUANTIFICATION AND STATISTICAL ANALYSIS
- DATA AND CODE AVAILABILITY

AUTHOR CONTRIBUTIONS

C.O. and N.D. conceived the project, analyzed data, prepared figures, and wrote the manuscript. C.O. performed and analyzed *in vitro* experiments. E.M.-T. performed CRISPRa and analyzed mutagenesis *in vivo*. C.L., J.B., and N.D. maintained mice and performed and analyzed *in vivo* experiments. N.H. and J.Zamudio analyzed sequencing data. J.Zimmer, J.S., and M.S. performed and analyzed nascent RNA sequencing (RNA-seq). E.T. performed subcellular fractionation. D.F. performed DNA-FISH.

DECLARATION OF INTERESTS

The authors declare no competing interests.

REFERENCES

Anders, S., Pyl, P.T., and Huber, W. (2015). HTSeq—a Python framework to work with high-throughput sequencing data. Bioinformatics *31*, 166–169.

Barsotti, A.M., Beckerman, R., Laptenko, O., Huppi, K., Caplen, N.J., and Prives, C. (2012). p53-dependent induction of PVT1 and miR-1204. J. Biol. Chem. *287*, 2509–2519.

Bassett, A.R., Akhtar, A., Barlow, D.P., Bird, A.P., Brockdorff, N., Duboule, D., Ephrussi, A., Ferguson-Smith, A.C., Gingeras, T.R., Haerty, W., et al. (2014). Considerations when investigating lncRNA function in vivo. eLife *3*, e03058.

Chaumeil, J., Augui, S., Chow, J.C., and Heard, E. (2008). Combined immunofluorescence, RNA fluorescent in situ hybridization, and DNA fluorescent in situ hybridization to study chromatin changes, transcriptional activity, nuclear organization, and X-chromosome inactivation. Methods Mol. Biol. *463*, 297–308.

Cho, S.W., Xu, J., Sun, R., Mumbach, M.R., Carter, A.C., Chen, Y.G., Yost, K.E., Kim, J., He, J., Nevins, S.A., et al. (2018). Promoter of lncRNA gene PVT1 is a tumor-suppressor DNA boundary element. Cell *173*, 1398–1412.e22.

Clarke, A.R., Gledhill, S., Hooper, M.L., Bird, C.C., and Wyllie, A.H. (1994). p53 dependence of early apoptotic and proliferative responses within the mouse intestinal epithelium following gamma-irradiation. Oncogene *9*, 1767–1773.

Conrad, T., and Ørom, U.A. (2017). Cellular fractionation and isolation of chromatin-associated RNA. Methods Mol. Biol. *1468*, 1–9.

Cory, S., Graham, M., Webb, E., Corcoran, L., and Adams, J.M. (1985). Variant (6;15) translocations in murine plasmacytomas involve a chromosome 15 locus at least 72 kb from the c-myc oncogene. EMBO J. *4*, 675–681.

Cui, M., You, L., Ren, X., Zhao, W., Liao, Q., and Zhao, Y. (2016). Long noncoding RNA PVT1 and cancer. Biochem. Biophys. Res. Commun. *471*, 10–14.

Dahlman, J.E., Abudayyeh, O.O., Joung, J., Gootenberg, J.S., Zhang, F., and Konermann, S. (2015). Orthogonal gene knockout and activation with a cata-lytically active Cas9 nuclease. Nat. Biotechnol. *33*, 1159–1161.

Dimitrova, N., Zamudio, J.R., Jong, R.M., Soukup, D., Resnick, R., Sarma, K., Ward, A.J., Raj, A., Lee, J.T., Sharp, P.A., and Jacks, T. (2014). LincRNA-p21 activates p21 in cis to promote Polycomb target gene expression and to enforce the G1/S checkpoint. Mol. Cell *54*, 777–790.

Dobin, A., Davis, C.A., Schlesinger, F., Drenkow, J., Zaleski, C., Jha, S., Batut, P., Chaisson, M., and Gingeras, T.R. (2013). STAR: ultrafast universal RNA-seq aligner. Bioinformatics *29*, 15–21.

DuPage, M., Dooley, A.L., and Jacks, T. (2009). Conditional mouse lung cancer models using adenoviral or lentiviral delivery of Cre recombinase. Nat. Protoc. *4*, 1064–1072.

Elling, R., Robinson, E.K., Shapleigh, B., Liapis, S.C., Covarrubias, S., Katzman, S., Groff, A.F., Jiang, Z., Agarwal, S., Motwani, M., et al. (2018). Genetic models reveal cis and trans immune-regulatory activities for lincRNA-Cox2. Cell Rep. *25*, 1511–1524.e6.

Engeland, K. (2018). Cell cycle arrest through indirect transcriptional repres-sion by p53: I have a DREAM. Cell Death Differ. *25*, 114–132.

Engreitz, J.M., Haines, J.E., Perez, E.M., Munson, G., Chen, J., Kane, M., McDonel, P.E., Guttman, M., and Lander, E.S. (2016). Local regulation of gene expression by lncRNA promoters, transcription and splicing. Nature *539*, 452–455.

Feldser, D.M., Kostova, K.K., Winslow, M.M., Taylor, S.E., Cashman, C., Whittaker, C.A., Sanchez-Rivera, F.J., Resnick, R., Bronson, R., Hemann, M.T., and Jacks, T. (2010). Stage-specific sensitivity to p53 restoration during lung cancer progression. Nature *468*, 572–575.

Graham, M., and Adams, J.M. (1986). Chromosome 8 breakpoint far 3′ of the c-myc oncogene in a Burkitt's lymphoma 2;8 variant translocation is equiva-lent to the murine pvt-1 locus. EMBO J. *5*, 2845–2851.

Graham, M., Adams, J.M., and Cory, S. (1985). Murine T lymphomas with retroviral inserts in the chromosomal 15 locus for plasmacytoma variant trans-locations. Nature *314*, 740–743.

Groff, A.F., Sanchez-Gomez, D.B., Soruco, M.M.L., Gerhardinger, C., Barutcu, A.R., Li, E., Elcavage, L., Plana, O., Sanchez, L.V., Lee, J.C., et al. (2016). In vivo characterization of linc-p21 reveals functional cis-regulatory DNA ele-ments. Cell Rep. *16*, 2178–2186.

Guan, Y., Kuo, W.L., Stilwell, J.L., Takano, H., Lapuk, A.V., Fridlyand, J., Mao, J.H., Yu, M., Miller, M.A., Santos, J.L., et al. (2007). Amplification of PVT1 con-tributes to the pathophysiology of ovarian and breast cancer. Clin. Cancer Res. *13*, 5745–5755.

Guo, J., Hao, C., Wang, C., and Li, L. (2018). Long noncoding RNA PVT1 mod-ulates hepatocellular carcinoma cell proliferation and apoptosis by recruiting EZH2. Cancer Cell Int. *18*, 98.

Hagège, H., Klous, P., Braem, C., Splinter, E., Dekker, J., Cathala, G., de Laat, W., and Forné, T. (2007). Quantitative analysis of chromosome conformation capture assays (3C-qPCR). Nat. Protoc. *2*, 1722–1733.

Ho, J.S., Ma, W., Mao, D.Y., and Benchimol, S. (2005). p53-dependent tran-scriptional repression of c-myc is required for G1 cell cycle arrest. Mol. Cell. Biol. *25*, 7423–7431.

Iwakawa, R., Takenaka, M., Kohno, T., Shimada, Y., Totoki, Y., Shibata, T., Tsuta, K., Nishikawa, R., Noguchi, M., Sato-Otsubo, A., et al. (2013). Genome-wide identification of genes with amplification and/or fusion in small cell lung cancer. Genes Chromosomes Cancer *52*, 802–816.

Jackson, E.L., Willis, N., Mercer, K., Bronson, R.T., Crowley, D., Montoya, R., Jacks, T., and Tuveson, D.A. (2001). Analysis of lung tumor initiation and pro-gression using conditional expression of oncogenic K-ras. Genes Dev. *15*, 3243–3248.

Jackson, E.L., Olive, K.P., Tuveson, D.A., Bronson, R., Crowley, D., Brown, M., and Jacks, T. (2005). The differential effects of mutant p53 alleles on advanced murine lung cancer. Cancer Res. *65*, 10280–10288.

Kim, H.P., Cho, G.A., Han, S.W., Shin, J.Y., Jeong, E.G., Song, S.H., Lee, W.C., Lee, K.H., Bang, D., Seo, J.S., et al. (2014). Novel fusion transcripts in human gastric cancer revealed by transcriptome analysis. Oncogene *33*, 5434–5441.

Kim, D., Langmead, B., and Salzberg, S.L. (2015). HISAT: a fast spliced aligner with low memory requirements. Nat. Methods *12*, 357–360.

Kong, R., Zhang, E.B., Yin, D.D., You, L.H., Xu, T.P., Chen, W.M., Xia, R., Wan, L., Sun, M., Wang, Z.X., et al. (2015). Long noncoding RNA PVT1 indicates a poor prognosis of gastric cancer and promotes cell proliferation through epigenetically regulating p15 and p16. Mol. Cancer *14*, 82.

Kopp, F., and Mendell, J.T. (2018). Functional classification and experimental dissection of long noncoding RNAs. Cell *172*, 393–407.

Kotzin, J.J., Spencer, S.P., McCright, S.J., Kumar, D.B.U., Collet, M.A., Mowel, W.K., Elliott, E.N., Uyar, A., Makiya, M.A., Dunagin, M.C., et al. (2016). The long non-coding RNA Morrbid regulates Bim and short-lived myeloid cell lifespan. Nature *537*, 239–243.

Lee, J.T. (2012). Epigenetic regulation by long noncoding RNAs. Science *338*, 1435–1439.

Levine, A.J., and Oren, M. (2009). The first 30 years of p53: growing ever more complex. Nat. Rev. Cancer *9*, 749–758.

Levy, N., Yonish-Rouach, E., Oren, M., and Kimchi, A. (1993). Complementation by wild-type p53 of interleukin-6 effects on M1 cells: induc-tion of cell cycle exit and cooperativity with c-myc suppression. Mol. Cell. Biol. *13*, 7942–7952.

Li, H., Handsaker, B., Wysoker, A., Fennell, T., Ruan, J., Homer, N., Marth, G., Abecasis, G., and Durbin, R.; 1000 Genome Project Data Processing Subgroup (2009). The Sequence Alignment/Map format and SAMtools. Bioinformatics *25*, 2078–2079.

Liberzon, A., Birger, C., Thorvaldsdóttir, H., Ghandi, M., Mesirov, J.P., and Tamayo, P. (2015). The Molecular Signatures Database (MSigDB) hallmark gene set collection. Cell Syst. *1*, 417–425.

Lin, C.Y., Lovén, J., Rahl, P.B., Paranal, R.M., Burge, C.B., Bradner, J.E., Lee, T.I., and Young, R.A. (2012). Transcriptional amplification in tumor cells with elevated c-Myc. Cell *151*, 56–67.

Love, M.I., Huber, W., and Anders, S. (2014). Moderated estimation of fold change and dispersion for RNA-seq data with DESeq2. Genome Biol. *15*, 550.

Martin, M. (2011). Cutadapt removes adapter sequences from high-throughput sequencing reads. EMBnet.journal *17*, 10–12.

Nagoshi, H., Taki, T., Hanamura, I., Nitta, M., Otsuki, T., Nishida, K., Okuda, K., Sakamoto, N., Kobayashi, S., Yamamoto-Sugitani, M., et al. (2012). Frequent PVT1 rearrangement and novel chimeric genes PVT1-NBEA and PVT1-WWOX occur in multiple myeloma with 8q24 abnormality. Cancer Res. *72*, 4954–4962.

Nikitin, A.Y., Alcaraz, A., Anver, M.R., Bronson, R.T., Cardiff, R.D., Dixon, D., Fraire, A.E., Gabrielson, E.W., Gunning, W.T., Haines, D.C., et al. (2004). Classification of proliferative pulmonary lesions of the mouse: recommenda-tions of the mouse models of human cancers consortium. Cancer Res. *64*, 2307–2316.

Northcott, P.A., Shih, D.J., Peacock, J., Garzia, L., Morrissy, A.S., Zichner, T., Stütz, A.M., Korshunov, A., Reimand, J., Schumacher, S.E., et al. (2012). Subgroup-specific structural variation across 1,000 medulloblastoma ge-nomes. Nature *488*, 49–56.

Pertea, M., Pertea, G.M., Antonescu, C.M., Chang, T.C., Mendell, J.T., and Salzberg, S.L. (2015). StringTie enables improved reconstruction of a tran-scriptome from RNA-seq reads. Nat. Biotechnol. *33*, 290–295.

Platt, R.J., Chen, S., Zhou, Y., Yim, M.J., Swiech, L., Kempton, H.R., Dahlman, J.E., Parnas, O., Eisenhaure, T.M., Jovanovic, M., et al. (2014). CRISPR-Cas9 knockin mice for genome editing and cancer modeling. Cell *159*, 440–455.

Porter, J.R., Fisher, B.E., Baranello, L., Liu, J.C., Kambach, D.M., Nie, Z., Koh, W.S., Luo, J., Stommel, J.M., Levens, D., et al. (2017). Global inhibition with specific activation: how p53 and MYC redistribute the transcriptome in the DNA double-strand break response. Mol. Cell *67*, 1013–1025 e9.

Riquelme, E., Suraokar, M.B., Rodriguez, J., Mino, B., Lin, H.Y., Rice, D.C., Tsao, A., and Wistuba, I.I. (2014). Frequent coamplification and cooperation

between C-MYC and PVT1 oncogenes promote malignant pleural mesothelioma. J. Thorac. Oncol. *9*, 998–1007.

Robinson, M.D., McCarthy, D.J., and Smyth, G.K. (2010). edgeR: a Bioconductor package for differential expression analysis of digital gene expression data. Bioinformatics *26*, 139–140.

Sachdeva, M., Zhu, S., Wu, F., Wu, H., Walia, V., Kumar, S., Elble, R., Watabe, K., and Mo, Y.Y. (2009). p53 represses c-Myc through induction of the tumor suppressor miR-145. Proc. Natl. Acad. Sci. U S A *106*, 3207–3212.

Schofield, J.A., Duffy, E.E., Kiefer, L., Sullivan, M.C., and Simon, M.D. (2018). TimeLapse-seq: adding a temporal dimension to RNA sequencing through nucleoside recoding. Nat. Methods *15*, 221–225.

Stewart, S.A., Dykxhoorn, D.M., Palliser, D., Mizuno, H., Yu, E.Y., An, D.S., Sabatini, D.M., Chen, I.S., Hahn, W.C., and Sharp, P.A. (2003). Lentivirus-delivered stable gene silencing by RNAi in primary cells. RNA *9*, 493–501.

Trapnell, C., Pachter, L., and Salzberg, S.L. (2009). TopHat: discovering splice junctions with RNA-Seq. Bioinformatics *25*, 1105–1111.

Tseng, Y.Y., and Bagchi, A. (2015). The PVT1-MYC duet in cancer. Mol. Cell. Oncol. *2*, e974467.

Tseng, Y.Y., Moriarity, B.S., Gong, W., Akiyama, R., Tiwari, A., Kawakami, H., Ronning, P., Reuland, B., Guenther, K., Beadnell, T.C., et al. (2014). PVT1 dependence in cancer with MYC copy-number increase. Nature *512*, 82–86.

Ventura, A., Kirsch, D.G., McLaughlin, M.E., Tuveson, D.A., Grimm, J., Lintault, L., Newman, J., Reczek, E.E., Weissleder, R., and Jacks, T. (2007). Restoration of p53 function leads to tumour regression in vivo. Nature *445*, 661–665.

Vousden, K.H., and Prives, C. (2009). Blinded by the light: the growing complexity of p53. Cell *137*, 413–431.

Xu, H., Luo, X., Qian, J., Pang, X., Song, J., Qian, G., Chen, J., and Chen, S. (2012). FastUniq: a fast de novo duplicates removal tool for paired short reads. PLoS ONE *7*, e52249.

Xu, M.D., Wang, Y., Weng, W., Wei, P., Qi, P., Zhang, Q., Tan, C., Ni, S.J., Dong, L., Yang, Y., et al. (2017). A positive feedback loop of lncRNA-*PVT1* and FOXM1 facilitates gastric cancer growth and invasion. Clin. Cancer Res. *23*, 2071–2080.

Xue, W., Chen, S., Yin, H., Tammela, T., Papagiannakopoulos, T., Joshi, N.S., Cai, W., Yang, G., Bronson, R., Crowley, D.G., et al. (2014). CRISPR-mediated direct mutation of cancer genes in the mouse liver. Nature *514*, 380–384.

Zeng, Y., Wang, T., Liu, Y., Su, Z., Lu, P., Chen, X., and Hu, D. (2017). LncRNA PVT1 as an effective biomarker for cancer diagnosis and detection based on transcriptome data and meta-analysis. Oncotarget *8*, 75455–75466.

Zhang, Y., Yang, G., and Luo, Y. (2019). Long non-coding RNA PVT1 promotes glioma cell proliferation and invasion by targeting miR-200a. Exp. Ther. Med. *17*, 1337–1345.

Zhao, L., Kong, H., Sun, H., Chen, Z., Chen, B., and Zhou, M. (2018). LncRNA-PVT1 promotes pancreatic cancer cells proliferation and migration through acting as a molecular sponge to regulate miR-448. J. Cell. Physiol. *233*, 4044–4055.

Zheng, X., Hu, H., and Li, S. (2016). High expression of lncRNA PVT1 promotes invasion by inducing epithelial-to-mesenchymal transition in esophageal cancer. Oncol. Lett. *12*, 2357–2362.

Zhu, S., Shuai, P., Yang, C., Zhang, Y., Zhong, S., Liu, X., Chen, K., Ran, Q., Yang, H., and Zhou, Y. (2017). Prognostic value of long non-coding RNA PVT1 as a novel biomarker in various cancers: a meta-analysis. Oncotarget *8*, 113174–113184.

STAR★METHODS

KEY RESOURCES TABLE

REAGENT or RESOURCE	SOURCE	IDENTIFIER
Antibodies		
Rabbit monoclonal (Y69) anti-c-myc	Abcam	Cat#ab32072; RRID: AB_731658
Mouse monoclonal anti-hsp90	BD Transduction Laboratories	Cat#610419; RRID: AB_397799
Rabbit monoclonal anti-hsp90	Cell Signaling Technologies	Cat#4877S; RRID: AB_2233307
Rabbit polyclonal anti-p53	Leica	Cat#P53-CM5P-L; RRID: AB_2744683
Rabbit Anti-Mouse IgG (H&L)	Abcam	Cat#ab46540; RRID: AB_2614925
Rabbit polyclonal anti-pHH3 Serine 10	Cell Signaling Technologies	Cat#9701S; RRID: AB_331535
Goat Anti-Mouse IgG (H + L)-HRP Conjugate	Bio-Rad	Cat#1706516; RRID: AB_11125547
Peroxidase AffiniPure Donkey Anti-Rabbit IgG (H+L)	Jackson ImmunoResearch	Cat#711-035-152; RRID: AB_10015282
Bacterial and Virus Strains		
Stable Competent E.coli (High Efficiency)	New England Biolabs	Cat#C3040H
5-alpha Competent E.coli (High Efficiency)	New England Biolabs	Cat#C2987U
Chemicals, Peptides, and Recombinant Proteins		
4-hydroxy tamoxifen	Cayman Chemical Company	Cat#17308-10
Doxorubicin hydrochloride	Sigma-Aldrich	Cat#D1515-10MG
Etoposide	Millipore Sigma	Cat#E1383-25MG
Cycloheximide	Sigma-Aldrich	Cat#C4859-1ML
Hexadimethrine bromide (polybrene)	Millipore Sigma	Cat#107689-10G
Puromycin dihydrochloride	Sigma-Aldrich	Cat#58-58-2
Hygromycin B	Roche	Cat#10843555001
DMEM, high glucose, pyruvate	GIBCO	Cat#11995065
Fetal Bovine Serum	Sigma-Aldrich	Cat#F0926-500ML
L-Glutamine	GIBCO	Cat#25030-081
Pen-strep	GIBCO	Cat#15140-122
NEAA	GIBCO	Cat#11140-050
2-mercaptoethanol	GIBCO	Cat#21985023
SYBR Fast Master Mix	Kapa Biosystems	Cat#kk4602
Nitrocellulose membranes	Bio-Rad	Cat#1620112
ECL Prime Western Blotting detection reagent	GE Healthcare	Cat#RPN2232
Methanol-free formaldehyde	Thermo Scientific	Cat#28908
cOmplete, Mini Protease Inhibitor Cocktail	Roche	Cat#4693124001
PureProteome Protein G Magnetic Beads	Millipore Sigma	Cat#LSKMAGG02
Salmon Sperm DNA	Invitrogen	Cat#15632011
Mouse Cot-1 DNA	Invitrogen	Cat#18440016
Proteinase K	Roche	Cat#03115879001
Formamide	Millipore Sigma	Cat#F9037-100ML
Stellaris® RNA FISH Hybridization Buffer	LGC Biosciences	Cat#SMF-HB1-10
Stellaris® RNA FISH Wash Buffer A	LGC Biosciences	Cat#SMF-WA1-60
Stellaris® RNA FISH Wash Buffer B	LGC Biosciences	Cat#SMF-WB1-20
VECTASHIELD® Antifade Mounting Medium with DAPI	Vector Laboratories	Cat#H-1200
Alexa Fluor® 488-5-UTP	Invitrogen	Cat#C11397

(Continued on next page)

REAGENT or RESOURCE	SOURCE	IDENTIFIER
Alexa Fluor® 594-5-UTP	Invitrogen	Cat#C11400
TRIzol Reagent	Invitrogen	Cat#15-596-018
TRIzol-LS Reagent	Invitrogen	Cat#10296028
RNasin Plus RNase inhibitor	Promega	Cat#N2615
CutSmart® Buffer	New England Biolabs	Cat#B7204S
BamHI-HF®	New England Biolabs	Cat#R3136L
T4 DNA Ligase	New England Biolabs	Cat#M0202L
Adenosine 5′-Triphosphate (ATP)	New England Biolabs	Cat#P0756L
4-thiouridine (s⁴U)	Alfa Aesar	Cat#AAJ60679MC
TURBO DNase	Invitrogen	Cat#AM2238
Agencourt RNAclean XP beads	Beckman Coulter	Cat#A63987
MTSEA biotin-XX	Biotium	Cat#900661
Critical Commercial Assays		
Mouse/Hepatocyte Nucleofector Kit	Lonza	Cat#VPL1004
RNeasy Mini Kit	QIAGEN	Cat#Q74106
High Capacity cDNA Reverse Transcription Kit	Applied Biosystems	Cat#Q74106
Zero Blunt TOPO PCR Cloning Kit	Invitrogen	Cat#450245
Nucleobond Xtra BAC kit	Takara Bio USA	Cat#740436.10
Nick Translation System	Invitrogen	Cat#18160-010
TruSeq Stranded mRNA Library Prep	Illumina	Cat#20020594
Clontech SMARTer Stranded Total RNA-Seq kit Pico Input Mammalian	Takara Bio USA	Cat#634411
Vectastain Elite ABC-HRP Kit (Peroxidase, rabbit IgG)	Vector Laboratories	Cat#PK-6101
DAB Peroxidase (HRP) Substrate Kit	Vector Laboratories	Cat#SK-4100
Deposited Data		
Raw and analyzed data of mouse cell lines	This study	GEO: GSE143204
Experimental Models: Cell Lines		
Mouse: Primary WT embryonic fibroblasts (MEFs)	This paper	N/A
Mouse: K-rasG12D/+; p53LSL/LSL; Rosa-CreERT2 (KPR8) cell line	Feldser et al., 2010	N/A
Mouse: p53LSL/LSL; Rosa-CreERT2 (p53-restorable MEFs)	Ventura et al., 2007	N/A
Mouse: 3TZ (3T3 derivative) cell line	T. Jacks, MIT	N/A
Human: fetal lung fibroblasts (TIG-1)	NIA Aging Cell Culture Repository	Cat#NG06173
Experimental Models: Organisms/Strains		
Mouse: Wild-type (WT) C57BL/6J	Jackson Laboratories	Cat#000664
Mouse: K-rasLSL-G12D/+ (K)	Jackson et al., 2001; Jackson Laboratories	Cat#008179
Mouse: p53FL/FL (P)	Jackson et al., 2005; Jackson Laboratories	Cat#008462
Mouse: Rosa26-Cas9LSL/LSL (C)	Platt et al., 2014; Jackson Laboratories	Cat#026556
Oligonucleotides		
qRT-PCR primers, see Table S1	This paper	N/A
PCR primers, see Table S1	This paper	N/A
smRNA FISH probes, see Table S1	This paper	see Table S1

Continued

REAGENT or RESOURCE	SOURCE	IDENTIFIER
3C qPCR primers, see Table S1	This paper	N/A
ChIP qPCR primers, see Table S1	This paper	N/A
ASO sequences, see Table S1	This paper	see Table S1
sgRNA sequences, see Table S1	This paper; Xue et al., 2014	N/A
dRNA sequences, see Table S1	This paper	N/A
Recombinant DNA		
pCMV-dR8.2 dvpr	Stewart et al., 2003	Addgene #8455
pCMV-VSV-G	Stewart et al., 2003	Addgene #8454
pWZL Hygro	S. Lowe, gift	Addgene #18750
BRD001	Broad Institute	N/A
BRD004	Broad Institute	N/A
UGPC	This paper	N/A
lenti-SAM-hygro	This paper	N/A
Myc BAC	BACPAC Resources Center	Cat#RP23-55F11
Chr 6 BAC	BACPAC Resources Center	Cat#RP24-301E22
Software and Algorithms		
GraphPad Prism, version 8.2.1 for MacOS	N/A	https://www.graphpad.com
Biorender	N/A	https://www.biorender.com
Tophat (v2.0.14)	Trapnell et al., 2009	http://ccb.jhu.edu/software/tophat/index.shtml
stringtie (v1.2.4)	Pertea et al., 2015	https://ccb.jhu.edu/software/stringtie/
HTSeq (v0.6.1)	Anders et al., 2015	https://htseq.readthedocs.io/en/release_0.11.1/
EdgeR (v3.22.3)	Robinson et al., 2010	https://bioconductor.org/packages/release/bioc/html/edgeR.html
FastUniq	Xu et al., 2012	https://sourceforge.net/projects/fastuniq/
Cutadapt (v1.16)	Martin, 2011	https://cutadapt.readthedocs.io/en/stable/
HISAT2 (v2.1.0)	Kim et al., 2015	https://ccb.jhu.edu/software/hisat2/index.shtml
SAMtools (v1.5)	Li et al., 2009	http://samtools.sourceforge.net
STAR (v2.5.3a)	Dobin et al., 2013	https://github.com/alexdobin/STAR
DEseq2	Love et al., 2014	https://bioconductor.org/packages/release/bioc/html/DESeq2.html

LEAD CONTACT AND MATERIALS AVAILABILITY

Further information and requests for resources and reagents should be directed to and will be fulfilled by the Lead Contact, Nadya Dimitrova (nadya.dimitrova@yale.edu). Plasmids generated in this study have been deposited to Addgene.

EXPERIMENTAL MODEL AND SUBJECT DETAILS

Mouse strains
All animal work was conducted in accordance with a protocol approved by the Yale University Institutional Animal Care and Use Committee. *K-ras*$^{LSL-G12D/+}$ *(K)* and *p53*$^{FL/FL}$ *(P)* mice were previously described (Jackson et al., 2001, 2005) and obtained from the laboratory of T. Jacks (MIT). *Rosa26-Cas9*$^{LSL/LSL}$ *(C)* mice were previously described (Platt et al., 2014) and purchased from Jackson Laboratories (026556). Wild-type (WT) C57BL/6J mice were purchased from Jackson Laboratories (000664). For irradiation experiments, 4-8 months-old mice were irradiated with 6 Gy of whole body irradiation and sacrificed 6 hours post irradiation. For tumor studies, 3-6 months-old mice were used. Experiments were performed blind to gender and with an equal distribution of males and females in each experimental group.

Cell culture and drug treatments

WT MEFs were isolated from embryos at E13.5 from timed matings of WT C57BL/6J animals. All MEF experiments were performed at passages 2-10. *KPR8* lung adenocarcinoma cell line of the genotype *K-ras*$^{G12D/+}$; *p53*$^{LSL/LSL}$; *Rosa-CreER*^{T2} was previously established from spontaneously arising primary tumors isolated from *K-ras*$^{LA2-G12D/+}$; *p53*$^{LSL/LSL}$; *Rosa-CreER*^{T2} mice, as previously described (Feldser et al., 2010). p53-restorable *p53*$^{LSL/LSL}$; *Rosa-CreER*^{T2} MEFs were previously described (Ventura et al., 2007). Genotypes and Tam-mediated restoration of p53 expression were validated by genotyping and by qRT-PCR and immunoblotting, respectively. Puromycin-sensitive *KPR8* (*KPR*) and p53-restorable MEF clones were generated by transient transfection with a guide RNA targeting the ORF of puromycin to inactivate the puromycin-resistance gene expressed from the Stop cassette, cloned downstream of a U6 promoter in a BRD004 lentiviral construct (a gift from the Broad Institute, MIT) that co-expresses spCas9 and GFP. Normal human fetal lung fibroblasts were purchased from the NIA Aging Cell Culture Repository (TIG-1, NG06173). Primary MEFs and human fibroblasts were maintained in DMEM (GIBCO) supplemented with 15% FBS (F0926, Sigma-Aldrich), 50 U/ml pen/strep (GIBCO), 2 mM L-glutamine (GIBCO), 0.1 mM non-essential amino acids (GIBCO), and 0.055 mM β-mercaptoethanol (GIBCO). Cancer cells and 293 viral packaging cells were cultured in DMEM supplemented with 10% FBS, 50 U/ml pen/strep, 2 mM L-glutamine, and 0.1 mM non-essential amino acids. All cell cultures were maintained at 37°C in a humidified incubator with 5% CO_2. Viral titering was performed in 3TZ cells, a derivative of 3T3 cells, expressing a LSL-LacZ transgene (generously provided by the laboratory of T. Jacks, MIT).

To delete the loxP-STOP-loxP (LSL) cassette preventing p53 expression, cells were treated with 0.5 μM 4-hydroxytamoxifen (Tam, Cayman Chemical Company). To induce DNA damage, cells were treated with 0.5 μM doxorubicin (Doxo, Sigma-Aldrich) or 50 μM etoposide (Etop, Millipore Sigma) for smRNA-FISH studies. To assess protein stability, cells were treated with 50 μg/ml cycloheximide (Chx, Sigma-Aldrich) for the indicated times.

Constructs

Mutagenesis of p53REs in cultured cells was performed with a gRNA targeting the p53RE of *Pvt1b* (gΔRE) or Gm26542 (g1 or g2), cloned downstream of a U6 promoter in BRD001 or BRD004 lentiviral constructs (gifts from the Broad Institute, MIT) that co-express spCas9 and either an IRES-driven puromycin-resistance gene or GFP, respectively. Control gRNA targeting dTomato (Con) was used as a negative control. Tumor-specific mutagenesis of p53REs *in vivo* was performed with gRNAs cloned downstream of a U6 promoter in UGPC (U6-gRNA-PGK-Cre) lentiviral vector. UGPC-Con targeting dTomato was used as a negative control. UGPC-p53KO targeting the ORF of p53 was used as a positive control (Xue et al., 2014). For CRISPRa experiments, a lentiviral vector (lenti-SAM-Hygro) was constructed to co-express nuclease-proficient spCas9, a U6-driven 15-mer 'dead RNA' (dRNA) extended by two MS2 loops (dRNA-MS2) (Dahlman et al., 2015), the transcriptional activator domains p65 and HSF1 fused to the MS2-binding protein (MBP), and a hygromycin-resistance gene. All sgRNA and dRNA sequences used in this study can be found in Table S1.

Lentivirus was produced in 293 cells by co-transfecting the lentiviral constructs with pCMV-dR8.2 dvpr (Addgene plasmid #8455) and pCMV-VSV-G (Addgene plasmid #8454) viral packaging constructs. Viral containing supernatants supplemented with 4 μg/ml polybrene (Millipore Sigma) were used to infect WT MEFs and *KPR* cells by 2-3 consecutive lentiviral infections, delivered at 24 hour-intervals. Following infections, cells were selected with 5 μg/ml (*KPR*) or 2 μg/ml (MEFs) puromycin (Sigma-Aldrich) or 800 μg/ml hygromycin (Roche). UGPC lentivirus was prepared as above, concentrated by ultracentrifugation, and titered by infecting 3TZ cells and determining the number of viral particles based on the fraction of LacZ-positive cells as previously described (DuPage et al., 2009).

Mutagenesis of the *Pvt1b* and Gm26542 p53REs was confirmed by PCR amplification of the region, subsequent cloning into pCR-Blunt II-TOPO® vector (Invitrogen) and Sanger sequencing.

For overexpression experiments, full-length *Pvt1a* (exon 1a-10) and *Pvt1b* (exon 1b-10) cDNAs were synthesized as gene blocks and cloned into pWZL Hygro retroviral vector (Addgene plasmid #18750). 5 μg of empty vector, *Pvt1a*-, or *Pvt1b*-expressing constructs were transfected into 1-3x10^6 WT MEFs using the Amaxa Mouse/Rat Hepatocyte Nucleofector Kit (Lonza, VPL-1004) and the Nucleofector 2b Device (Lonza). Analysis was performed at 48 hours post transfection.

METHOD DETAILS

RNA isolation and qRT-PCR

For RNA-seq and qRT-PCR analysis, RNA was isolated with the RNeasy Mini Kit (QIAGEN) and 0.5-1 μg of total RNA was reverse transcribed using the High Capacity cDNA Reverse Transcription Kit (Applied Biosystems). SYBR Green PCR master mix (Kapa Biosystems) was used for quantitative PCR in triplicate reactions with primers listed in Table S1. Relative RNA expression levels were calculated using the ddCt method compared to GAPDH and normalized to control samples.

Immunoblotting

Cells were collected, counted, and lysed in 2 × Laemmli buffer (100 mM Tris-HCl pH6.8, 200 mM DTT, 3% SDS, 20% glycerol) at 0.5-1x10^4 cells/μl. Samples were heated at 95°C for 7 minutes and passed through an insulin syringe. Protein from 1x10^5 cells was separated on 10% SDS-polyacrylamide gels and transferred to nitrocellulose membranes (Bio-Rad). After blocking (5% milk, PBST), membranes were incubated overnight at 4°C in primary antibody, then 1hr at RT in secondary antibody. The following antibodies

were used: anti-c-Myc (1:1000, clone Y69, ab32072, Abcam), anti-Hsp90 (1:2500, 610419, BD Transduction Laboratories), anti-Hsp90 (1:1000, 4877S, Cell Signaling Technology), goat anti-mouse secondary antibody (1:50000, 1706516, Bio-Rad), and donkey anti-rabbit secondary antibody (1:50000, 711-035-152, Jackson ImmunoResearch). Protein bands were visualized using Amersham ECL Prime Western Blotting Detection Reagent (GE Healthcare). Quantification of Myc and Hsp90 protein levels was performed using the rectangle selection and measure tools in FIJI and Myc levels plotted relative to Hsp90 levels and normalized to negative control in relevant graphs. For cycloheximide experiments, Myc levels were normalized to negative control and half-life of Myc protein was determined using Prism8 software.

Chromatin immunoprecipitation (ChIP)

Cells were harvested by trypsinization, counted, washed once in PBS and crosslinked in 1% methanol-free formaldehyde (Thermo Scientific) diluted in PBS for 10 min at RT. The reaction was stopped by adding glycine to a final concentration of 100 mM and placing the samples on ice for 5 min. Cells were washed twice in cold PBS and the pellet was frozen and stored at −80°C.

5-10x10^6 nuclei were isolated by incubating the thawed cell pellet in Cell lysis buffer (20 mM Tris-HCl, pH 8.0, 85 mM KCl, 0.5% NP-40), supplemented with protease inhibitors (1 mM PMSF and Mini Complete Protease Inhibitor Cocktail Tablet, Roche) on ice for 10 min. After centrifugation, the supernatant was removed and the nuclei were resuspended in Nuclei lysis buffer (50 mM Tris-HCl, pH 8.0, 10 mM EDTA, 1% SDS supplemented with protease inhibitors) and incubated for 10 min on ice. Next, chromatin was sonicated to 300-500 bp fragment size in an ice-water slurry for 10 cycles (15" ON, 30" OFF) using a Bioruptor sonicator (Diagenode). Sonicated lysates were centrifuged at 13K rpm for 20 min and diluted in ChIP dilution buffer (0.01% SDS, 1.1% Triton- X100, 1.1 mM EDTA, 20 mM Tris-HCl, pH 8.0, 167 mM NaCl, supplemented with protease inhibitors). Input aliquots were saved at this point. The sonicated chromatin was precleared with beads (PureProteome Protein G Magnetic Beads, Millipore Sigma) and used to set up chromatin immunoprecipitations with a p53 antibody (P53-CM5P-L, Leica), or control IgG (ab46540, Abcam) and incubated overnight at 4°C on a rotator. Beads (PureProteome Protein G Magnetic Beads, Millipore Sigma) were blocked overnight in 1% BSA in PBS supplemented with 20 μg salmon sperm DNA (Invitrogen) per immunoprecipitation reaction. The next day, the blocked beads were added to the immunoprecipitation reactions and samples were incubated on the rotator for an additional hour. Beads were washed once in each of the following washes for 5 min at 4°C on the rotator: Low salt wash (0.1% SDS, 1% Triton X-100, 2 mM EDTA, 20 mM Tris-HCl pH 8.0, 150 mM NaCl supplemented with protease inhibitors), High salt wash (0.1% SDS, 1% Triton X-100, 2 mM EDTA, 20 mM Tris-HCl, pH 8.0, 500 mM NaCl), LiCl wash (0.25 M LiCl, 1% NP-40, 1% Na deoxycholate, 1 mM EDTA, 20 mM Tris-HCl, pH 8.0), and TE wash (10 mM Tris-HCl, pH 8.0, 1 mM EDTA).

After completely removing any remaining liquid from the washes, beads were resuspended in Elution buffer (50 mM Tris-HCl, pH 8.0, 10 mM EDTA, pH 8.0, 1% SDS) and incubated at 65°C for 15 min with frequent vortexing to prevent settling. After elution, the beads were pelleted, and the supernatant was transferred to a new tube and incubated overnight at 65°C to reverse the crosslinking. The next day, samples were treated with RNaseA or 2 hours at 37°C, followed by a proteinase K (Roche) treatment for 30 min at 55°C. The DNA was purified by phenol-chloroform extraction and EtOH precipitation. The DNA pellet was air-dried, resuspended in 200 μL H$_2$O and used for quantitative PCR analysis (ChIP-qPCR) using primers listed in Table S1.

Single-molecule FISH (smRNA-FISH)

Quasar570 (Q570)- and Quasar670 (Q670)-conjugated Stellaris FISH probes are listed in Table S1 (Stellaris, LGC Biosciences). smRNA-FISH was performed according to the manufacturer recommendations. Briefly, cells were grown on coverslips and fixed for 10 min in 4% methanol-free formaldehyde (Thermo Scientific) at RT, followed by PBS washes. Cells were dehydrated overnight at 4°C in 70% EtOH (diluted in DEPC-H$_2$O) and stored in 70% EtOH for up to a week at 4°C. Coverslips were transferred to a hybridization chamber and equilibrated for 5 min in Wash Buffer A (Stellaris, LGC Biosciences) prepared with formamide (Millipore Sigma) according to manufacturer's instructions. Cells were incubated overnight at 30°C with the indicated probes diluted 1:50 in Hybridization solution (Stellaris, LGC Biosciences) prepared with formamide according to manufacturer's instructions. The next day, cells were washed 2 times for 30 min at 30°C in Wash Buffer A, incubated in Wash Buffer B (Stellaris, LGC Biosciences) for 5 min at RT, and mounted in antifade reagent (Vectashield Mounting medium with DAPI, Vector Laboratories). The following probesets were used: *Pvt1b (ex.1b)* detecting *Pvt1b* isoform with 10 probes spanning exon 1b, labeled with Q670 and false-colored in red; *Pvt1a (ex.1a)* detecting *Pvt1a* isoform with 11 probes spanning exon 1a, labeled with Q670 and false-colored in red; *Pvt1 (ex.1a-10)* detecting total *Pvt1* with 48 probes spanning exons 1a-10, labeled with Q570 and false-colored in green; *Pvt1 (introns)* detecting nascent *Pvt1a* with 31 probes spanning intron 1 upstream of exon 1b, labeled with Q670 and false-colored in red; and *Myc (intron)* detecting nascent *Myc* with 33 probes spanning intron 1 of *Myc*, labeled with Q570 and false-colored in green. *Pvt1a (ex.1a)* and *Pvt1b (ex.1b)* probesets do not detect at the single molecule level. Images were captured using an Axio Imager 2 microscope system (Zeiss) with a PlanApo 63x 1.4 oil DIC objective lens (Zeiss). For *KPR* cells, z stacks of 12 planes at 0.5 μm steps were acquired and used to generate maximum intensity projections. For WT MEFs, single plane images were acquired. All images were edited using Adobe Photoshop.

DNA-Fluorescence *in situ* hybridization (FISH)

DNA-FISH was performed as previously described (Chaumeil et al., 2008). To generate probes, the following BAC clones were used: RP23-55F11 (Myc) and RP24-301E22 (Chr 6) (BACPAC Resources). BAC DNA was purified with a Nucleobond Xtra BAC kit (Takara Bio USA) and nick translated with a nick translation system (Invitrogen) and Alexa Fluor® 488-5-UTP or Alexa Fluor® 594-5-UTP

(Invitrogen) following manufacturer instructions. Final probes were ethanol precipitated with 7.5M ammonium acetate and stored in sterile TE at −20°C.

20 ng of nick-translated probe was precipitated with 3 μg of salmon sperm DNA (Invitrogen) and 1 μg of mouse COT1 DNA (Invitrogen) using 1/10th volume of sodium acetate (3M, pH 5.5) and 2.5 volumes of ethanol. Probes were stored overnight at −20°C, then centrifuged at 13K rpm for 30 min at 4°C, washed twice with 70% ethanol, and air-dried. Pellets were resuspended in formamide (Millipore Sigma), incubated at 37°C for at least 10 min, and denatured for 7 min at 75°C. After denaturing, an equal volume of 2X hybridization buffer (4X SSC, 20% w/v dextran sulfate, 2 mg/mL BSA, 40 mM RVC) was added and probe-DNA mixtures were pre-annealed for 30 min to 1 hour at 37°C.

Cells were plated on coverslips and fixed in 4% paraformaldehyde in PBS for 10 min at RT, followed by PBS washes. Cells were permeabilized in 0.5% Triton X-100 in PBS for 6 min, washed twice with 70% ethanol and stored in 70% ethanol at −20°C. Coverslips were dehydrated in an ethanol series (80%, 90%, 100%), air-dried, and incubated in RNase A diluted in 2X SSC (100 μg/mL) for 1 hour at 37°C. Coverslips were washed three times with 2X SSC for 5 min and incubated in 50 μg/mL pepsin diluted into prewarmed 0.01M HCl for 3 min at 37°C, followed by two 5 min PBS washes and one in 1X PBS/MgCL$_2$. After washing, coverslips were incubated in 1% formaldehyde (Thermo Scientific) in 1X PBS/MgCL$_2$ for 10 min at RT. Coverslips were next washed in PBS for 5 min and dehydrated in an ethanol series (70%/90%/100%) and air-dried. Coverslips were then denatured in prewarmed 50% formamide in 2X SSC for 30 min at 80°C, dehydrated in an ice-cold ethanol series (70%/90%/100%), and incubated with denatured probe DNA overnight at 42°C in a dark chamber humidified with 50% formamide in 2X SSC. Following incubation, coverslips were washed three times with prewarmed 50% formamide in 2X SSC at 42°C for 5 min and three times with prewarmed 2X SSC at 42°C for 5 min. Coverslips were mounted on slides with antifade mounting medium with DAPI (Vector Laboratories) and sealed with nail polish. Single plane images were captured using an Axio Imager 2 microscope system (Zeiss) with a PlanApo 63x 1.4 oil DIC objective lens (Zeiss).

Subcellular fractionation

Subcellular fractionation was performed as previously described (Conrad and Ørom, 2017) with slight modifications. Briefly, cells were harvested by trypsinization, rinsed once in PBS and re-suspended in 1 mM EDTA in PBS. 1x10^6 cells were set aside for whole cell (WC) RNA isolation using TRIzol (Invitrogen) following the manufacturer's protocol. 3 x10^6 cells were lysed in 0.4 mL cell lysis buffer (10 mM TrisHCl pH 7.5, 0.15% NP-40, 150 mM NaCl, 100 U/mL RNase-IN (Promega)) for 5 min on ice. Lysate was layered on a sucrose cushion (24% w/v sucrose, 150 mM NaCl, 10 mM TrisHCl pH 7.5,100 U/mL RNase-IN) and centrifuged for 10 min at 3,500 g, yielding the cleared cytoplasmic fraction (supernatant) and pelleted nuclei. Nuclear pellets were washed once in PBS supplemented with 1 mM EDTA, re-suspended in 0.25 mL glycerol buffer (50% glycerol, 20 mM Tris-HCl pH 7.5, 75 mM NaCl, 0.5 mM EDTA, 0.85 mM DTT, 100 U/mL RNase-IN), and lysed by the immediate addition of an equal volume nuclear lysis buffer (10 mM HEPES pH 7.6, 7.5 mM MgCl$_2$, 0.2 mM EDTA, 300 mM NaCl, 1% NP-40, 1 mM DTT, 1M Urea, 100 U/mL RNase-IN) with 2 min incubation on ice. Centrifugation for 2 min at 18,800 g yielded the nucleoplasmic and chromatin- associated fractions in the supernatant and pellet, respectively. Chromatin pellets were washed once in 1 mM EDTA in PBS and solubilized in 1 mL TRIzol reagent by syringing. RNA was extracted from the cytoplasmic and nucleoplasmic fractions using TRIzol-LS (Invitrogen) and from the chromatin-associated fraction using TRIzol following the manufacturer's protocols. Subcellular RNA enrichment patterns were determined by qRT-PCR, normalizing fraction Ct values to WC Ct values. Cytoplasmically-enriched RNA *Rn7s1* and chromatin-enriched RNA *Kcnq1ot1* served as fractionation quality controls. Primer sequences can be found in Table S1.

Antisense knockdown

1 μM *Pvt1*-targeting (ASO1, ASO2, and ASO3) or control (CON) antisense LNA Gapmers (Exiqon, QIAGEN) were transfected into 1-3x10^6 MEFs using the Amaxa Mouse/Rat Hepatocyte Nucleofector Kit (Lonza, VPL-1004) and the Nucleofector 2b Device (Lonza). Knockdown of *Pvt1* variants and the corresponding effects on *p21* and *Myc* expression were assayed at 72 hours post-transfection by qRT-PCR following the indicated treatments. The sequences of all ASOs are listed in Table S1.

Chromosome Conformation Capture (3C)

Chromosome conformation capture was performed as described previously with minor modifications (Hagège et al., 2007). Briefly, cells were harvested by trypsinization, counted, washed once in PBS and 5-10x10^6 cells were crosslinked in 1% methanol-free formaldehyde (Thermo Scientific) diluted in PBS for 10 min at RT. The reaction was stopped by adding 1.425 mL of 1 M glycine. Cell pellets were frozen in a bath of dry ice covered in 100% EtOH and stored at −80°C, or were processed immediately. Cells were lysed in 5 mL cell lysis buffer (20 mM TrisHCl pH8.0, 85 nM KCl, 0.5% NP-40, 5 mM MgCl$_2$, 0.1 mM EGTA) including 1x complete protease inhibitor (Roche). Cell nuclei were resuspended in 0.5 mL of 1.2x Cutsmart restriction buffer (New England Biolabs) and SDS was added to each tube to a final concentration of 0.3%. Following extraction with 2% Triton X-100, chromatin was digested overnight at 37°C with 400-800 U BamHI-HF (New England Biolabs). Ligations were performed in a total reaction volume of 6.125 mL of 1.15x ligation buffer (10x Ligation Buffer: 600 mM Tris-HCl pH7.5, 50 mM DTT, 50 mM MgCl$_2$, 10 mM ATP (New England Biolabs)) using 100 U of T4 DNA ligase (New England Biolabs) with incubation at 16°C for 4 h, followed by further incubation at RT for 30 min. Reversal of crosslinking was performed by adding 300 μg proteinase K (Roche) followed by incubation at 65°C overnight. DNA was extracted with phenol-chloroform followed by EtOH precipitation. The efficiency of restriction enzyme digestion was examined using qRT-PCR with primer sets spanning BamHI sites. The concentrations of 3C libraries were determined by qRT-PCR and compared to a genomic

DNA reference of known concentration. Samples were subsequently diluted to a concentration of 20 ng/μl and a total of 50 ng was used for each qRT-PCR reaction. Interaction frequencies were determined using a unidirectional primer strategy with an anchor designed against the promoter of *Myc* (A1) and were normalized to a control region in the *Myc-Pvt1* locus. The primer sequences can be found in Table S1.

RNA-seq

Total RNA was isolated in three biological replicates. PolyA selection and cDNA library preparation was performed using TruSeq Stranded mRNA Library Prep (Illumina). Paired-end 100 bp sequencing was performed on an Illumina HiSeq 4000 instrument. RNA-seq read files were merged from technical replicates and mapped to the mm10 genome assembly using Tophat (ver 2.0.14) (Trapnell et al., 2009) with gencode (vM10) annotation used as the transcriptome index. Additional transcripts were assembled using stringtie (1.2.4) (Pertea et al., 2015) and reads within exon sequences counted using HTSeq (HTSeq-0.6.1) counts (Anders et al., 2015). The differential expression analysis was performed with EdgeR (3.22.3) (using general linear model settings for biological triplicates with blocked matrix model for paired comparisons) (Robinson et al., 2010). For analysis of Myc targets, the Hallmark Gene Set in the Molecular Signature Database (Broad Institute) (Liberzon et al., 2015) was used and compared to randomly selected and expression matched genes with statistical significance of differential expression determined with a Kolmogorov-Smirnov test.

Transcriptome-wide TimeLapse-seq

At approximately 60% cellular confluence, media was spiked with a final concentration of 100 μM s⁴U (Alfa Aesar) and grown in the dark for 1 hour. Cells were rinsed once with PBS, scraped from plates, suspended in 1 mL TRIzol (Invitrogen), and frozen overnight at −80°C. Total RNA was purified and treated with TimeLapse chemistry essentially as described (Schofield et al., 2018) with minor modifications. Briefly, following chloroform extraction and isopropanol precipitation (supplemented with 1 mM DTT) genomic DNA was depleted by treating with TURBO DNase (Invitrogen) and total RNA was extracted with acidic phenol:chloroform:isoamyl alcohol and EtOH precipitation. Isolated total RNA was mixed with 600 mM TFEA, 1 mM EDTA and 100 mM sodium acetate, pH 5.2 in water. A solution of 10 mM NaIO₄ was added and the reaction mixture was incubated at 45°C for 1 hr. Chemically treated RNA was purified using Agencourt RNAclean XP beads (1 equivalent volume, Beckman Coulter) according to manufacturer's instructions. Purified material was then incubated in a reducing buffer (10 mM DTT, 100 mM NaCl, 10 mM Tris pH 7.4, 1 mM EDTA) at 37°C for 30 min, followed by a second RNAclean bead purification. For each sample, 10 ng of total RNA input was used to prepare sequencing libraries from the Clontech SMARTer Stranded Total RNA-Seq kit Pico Input (Takara Bio USA) with ribosomal cDNA depletion. Paired-end 100 bp sequencing was performed on an Illumina HiSeq 4000 instrument.

TT-TimeLapse-seq

At approximately 60% cellular confluence, media was spiked with s⁴U (1 μM final, Alfa Aesar) and cells were grown in the dark for 5 min. Total RNA and DNA isolation were performed as described above. Total RNA (50 μg) was biotinylated with MTSEA biotin-XX (Biotium), isolation and streptavidin enrichment essentially as described (Schofield et al., 2018). Enriched RNA was chemically treated as described above. Library construction and sequencing were performed essentially as described above.

TimeLapse-seq mutational analysis

Filtering and alignment to the mouse GRCm38.p5 were performed essentially as described previously (Schofield et al., 2018). Briefly, reads were filtered to remove duplicate sequences with FastUniq (Xu et al., 2012), trimmed of adaptor sequences with Cutadapt v1.16 (Martin, 2011) and aligned to GRCm38 using HISAT2 v2.1.0 (Kim et al., 2015) (with default parameters except -mp 4,2). Reads aligning to transcripts were quantified with HTSeq (Anders et al., 2015) htseq-count. SAMtools v1.5 (Li et al., 2009) was used to collect only read pairs with a mapping quality greater than 2 and concordant alignment (sam FLAG = 147/99 or 83/163). Mutation calling was performed essentially as described previously (Schofield et al., 2018). Briefly, T-to-C mutations were only considered if they met several conditions. Mutations must have a base quality score greater than 40 and be more than 3 nucleotides from the read's end. Sites of likely single-nucleotide polymorphisms (SNPs) and alignment artifacts were identified with bcftools or from sites of high mutation levels in the non-s⁴U treated controls and were not considered in mutation calling. Browser tracks were made using STAR v2.5.3a (Dobin et al., 2013) and normalized across samples using scale factors calculated using RNA-seq reads using edgeR (Robinson et al., 2010) (calcNormFactors using method = 'upperquartile').

Differential expression analysis

Differential expression analysis of transcriptome-wide TimeLapse-seq and TT-TimeLapse-seq data was performed with DESeq2 (Love et al., 2014) essentially as described previously (Schofield et al., 2018). DESeq2 expression analysis was performed on TT-TimeLapse-seq and transcriptome-wide TimeLapse-seq data to determine changes in transcriptional activity and mRNA expression, respectively.

Growth curve and colony assay

To generate growth curves, Con-, ΔRE-, sg1-, or sg2-expressing *KPR* cells were grown in the presence or absence of Tam. Population doublings over indicated time course were plotted as the average of three independent experiments. For colony assays,

4x10^5 Con- or ΔRE -expressing *KPR* cells were plated in the presence of Tam in 6 cm dishes and monitored for colony formation. Plates were washed with PBS, fixed in 0.5% Crystal Violet; 25% MeOH for 10 minutes and washed in ddH$_2$O. The average of three biological replicates is shown.

Tumor studies

Lung tumorigenesis was initiated in cohorts of *KC* and *KPC* mice as described in (DuPage et al., 2009) by intratracheal infection with 1x10^5 pfu UGPC lentiviruses . Mice were analyzed at 12 or 16 weeks post tumor initiation. For histological analyses, lungs were inflated with 4% paraformaldehyde, and fixed overnight in 4% paraformaldehyde, prior to dehydration in 70% ethanol. Fixed lungs were embedded in paraffin, sectioned, and stained with hematoxylin and eosin (H&E). Tumor burden scored as tumor area relative to total lung area was determined using the freehand selection tool and Measure feature in ImageJ on images acquired with an Axio Imager 2 microscope system (Zeiss) with a PlanApo 10x 0.3 objective lens (Zeiss). Tumor grade was scored as previously described (DuPage et al., 2009; Nikitin et al., 2004).

Immunohistochemistry

Immunohistochemistry on paraffin sections was performed using the ABC Vectastain kit (Vector Labs) with an antibody to pHH3 Serine 10 (9701S, Cell Signaling Technologies). The staining was visualized with DAB (Vector Labs) and slides were counterstained with hematoxylin.

QUANTIFICATION AND STATISTICAL ANALYSIS

In relevant figures, figure legends convey the statistical details of experiments including statistical tests used and type and number (*n*) of biological replicates, while asterisks define degree of significance as described. All Student's t tests and Mann-Whitney *U*-tests were analyzed in two sided. All sequencing data were aligned to the mouse genome (GRCm38/mm10). All statistical analyses were performed and graphics were generated using Prism8 software.

DATA AND CODE AVAILABILITY

All software used in this study is listed in the Key Resources Table. Data generated in this study are available through Gene Expression Omnibus (GEO) under accession number GEO: GSE143204. Graphical abstract was created using graphics from https://www.biorender.com.

Supplemental Information

p53 Activates the Long Noncoding RNA *Pvt1b*

to Inhibit *Myc* and Suppress Tumorigenesis

Christiane E. Olivero, Elena Martínez-Terroba, Joshua Zimmer, Clara Liao, Ephrath Tesfaye, Nima Hooshdaran, Jeremy A. Schofield, Jordan Bendor, Dorthy Fang, Matthew D. Simon, Jesse R. Zamudio, and Nadya Dimitrova

Olivero et al. Figure S1

A

KPR: Copies/cell
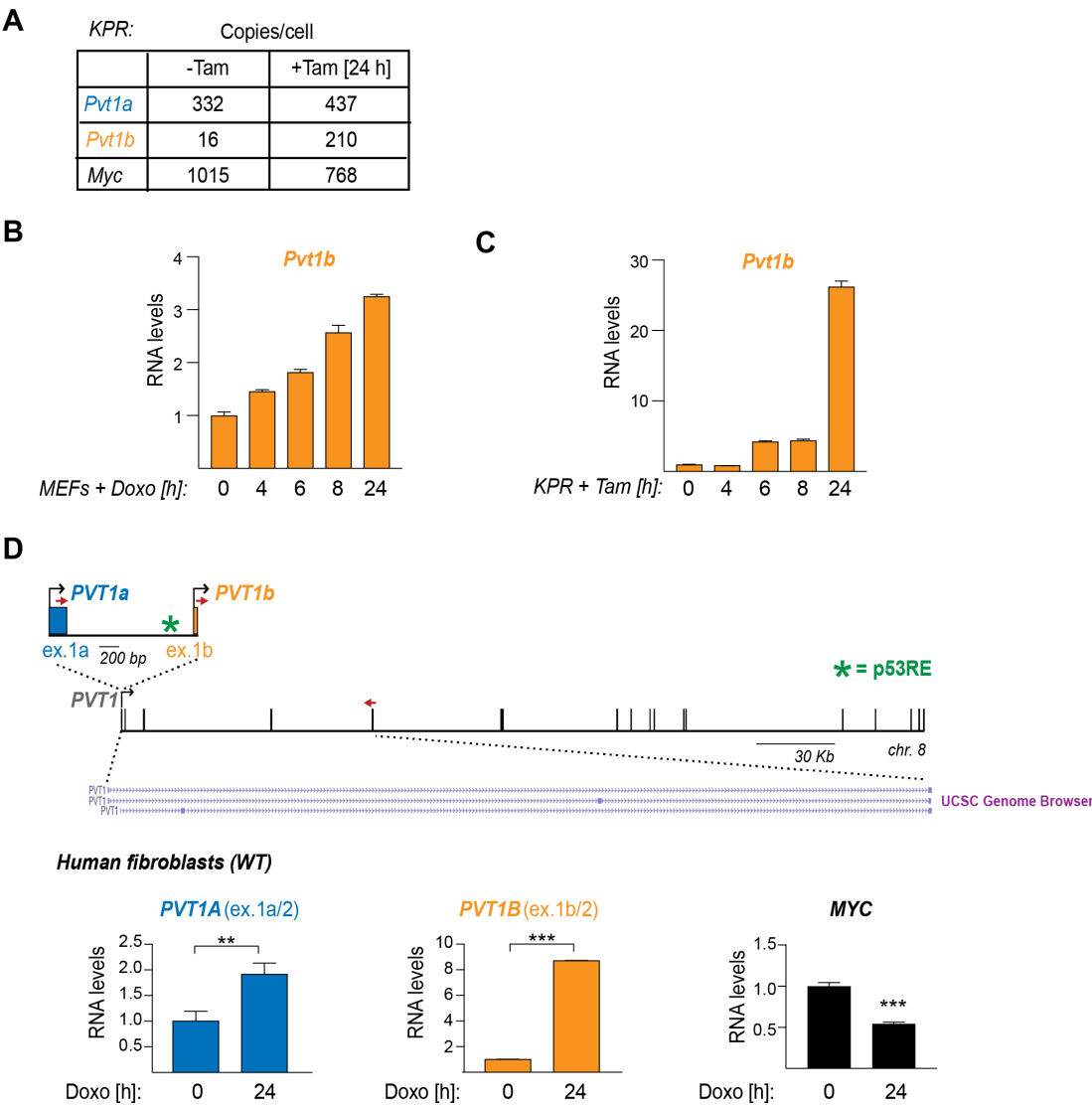
	-Tam	+Tam [24 h]
Pvt1a	332	437
Pvt1b	16	210
Myc	1015	768

B

MEFs + Doxo [h]:   0 4 6 8 24

C

KPR + Tam [h]:   0 4 6 8 24

D

Human fibroblasts (WT)

Figure S1. p53 activates the lncRNA isoform *Pvt1b*, Related to Figure 2.
(A) Copy number calculations of *Pvt1a*, *Pvt1b*, and *Myc* by qRT-PCR analysis of *KPR* cells untreated or 24 h post-treatment with Tam.
(B, C) qRT-PCR analysis of *Pvt1b* levels in (B) MEFs treated with Doxo for the indicated times and (C) *KPR* cells treated with Tam for the indicated times. The observed induction of *Pvt1b* as early as 4-6 hours post stress suggests direct transcriptional activation by p53.
(D) *Top* Schematic of the human *PVT1* locus, highlighting exon 1a (blue), exon 1b (orange), the conserved p53RE (green star) and showing the location of qPCR primers (red arrows), *Bottom* qRT-PCR analysis of relative *PVT1A*, *PVT1B,* and *MYC* RNA levels in normal human fibroblasts untreated or treated with Doxo for 24 h. Data show the mean ± SEM of 3 technical replicates from a representative example of two biological replicates.
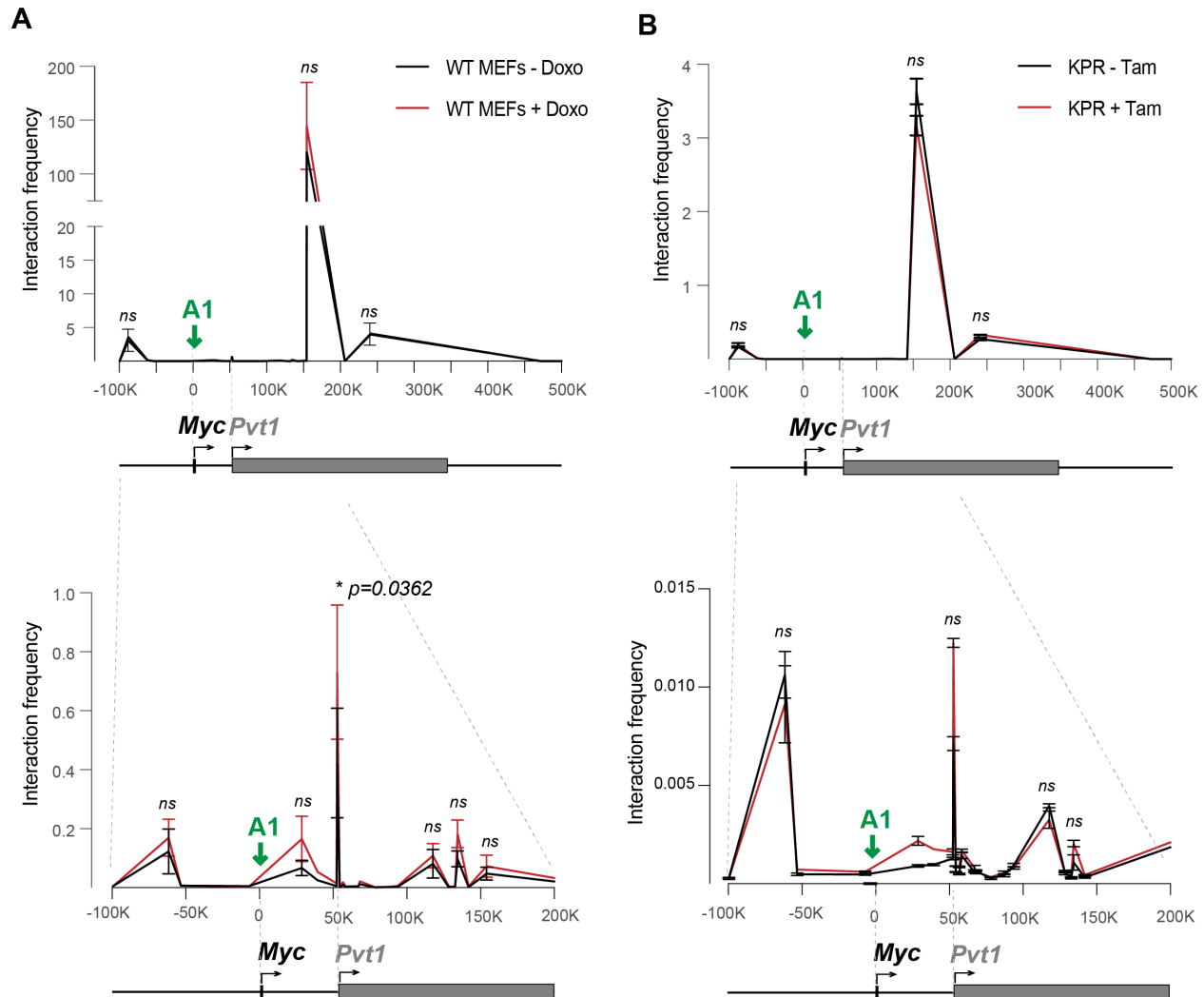
Figure S2. p53 activation does not substantially alter chromatin architecture of the *Myc-Pvt1* locus, Related to Figure 2.
(A-B) 3C analysis of BamHI-digested DNA from (A) WT MEFs, untreated or treated for 24 h with Doxo and (B) *KPR* cells, untreated or treated for 24 h with Tam. Interaction frequency with an anchor in the M*yc* promoter (A1, green arrow) is plotted relative to genomic location. A unidirectional forward primer strategy was used to probe chromatin interactions within the *Myc-Pvt1* locus and primers were designed to query previously described enhancer regions interacting with the *Myc* promoter (Cho et al., Cell 2018), published H3K4me1 peaks (Meyer et al., JBC 2016), and control regions. *Top* Interaction frequency plots depicting the strongest interactions between the *Myc* promoter and upstream and downstream enhancers. Note that the chromatin architecture is largely unchanged by the presence of stress. *Bottom* Interaction frequency plot depicting weaker interactions between the *Myc* promoter and upstream and downstream enhancers. Note the change of scale and that the three strongest peaks, depicted

in the *Top* panels, are excluded in the *Bottom* panels to allow visualization of smaller peaks. Note that there is a pre-existing chromatin looping interaction between the *Myc* and *Pvt1* promoters, which exhibits a mild increase following Doxo treatment in (A) WT MEFs but is not significantly changed in (B) Tam-treated compared to untreated *KPR* cells. Data represent (A) n=3 biological replicates or (B) representative plot from n=2 biological replicates, ns = not significant, *p<0.05, paired t-test.

A

	Pvt1a (ex.1a)	*Pvt1 (ex.1a-10)*	Merge+DAPI
WT - Etop			
WT + Etop			

B

	Pvt1a (ex.1a)	*Pvt1 (ex.1a-10)*	Merge+DAPI
KPR - Tam			
KPR + Tam			

C

	Myc BAC	*Chr 6 BAC*	Merge+DAPI
MEFs			
KPR			
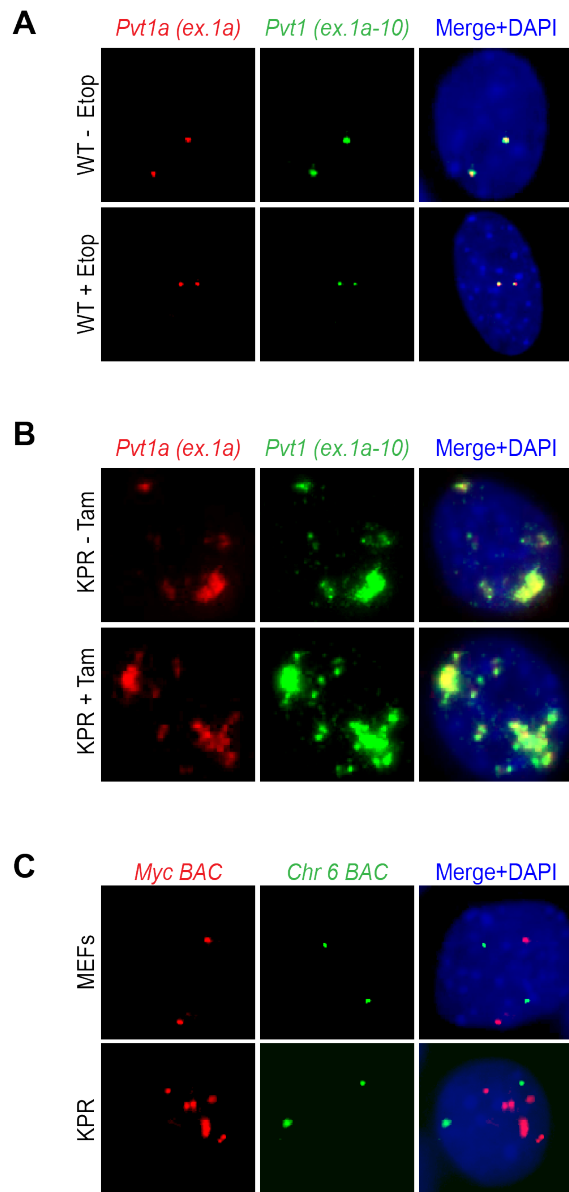
Figure S3. Co-localization of *Pvt1*a and total *Pvt1* by smRNA-FISH, Related to Figure 3.
(A-B) smRNA-FISH with probes designed against indicated regions in (A) WT MEFs, untreated or treated with Etop for 24 h and in (B) *KPR* cells untreated or treated with Tam for 24 h. The following probesets are shown: *Pvt1a (ex.1a, red)* detecting *Pvt1a* isoform with 11 probes spanning exon 1a and *Pvt1 (ex.1a-10, green)* detecting total *Pvt1* with 48 probes spanning exons 1a-10. Note: The *Pvt1a* probeset does not detect at the single molecule level.
(C) DNA-FISH with probes generated using a Bacterial Artificial Chromosome (BAC) of the Myc locus (*Myc BAC, red*) or a control region in chromosome 6 (*Chr 6 BAC, green*) in untreated WT MEFs and *KPR* cells, highlighting increased copy number of the *Myc* locus in *KPR* cells.

Olivero et al. Figure S4

A

Doxo: - + - +
ASO: CON   1

B

Enrichment at p53RE

p53 ChIP

ns

ASO: CON 1

C

dRNA-MS2: C A1 A2 C A1 A2
KPR: - Tam   + Tam

D

EV   1a   1b
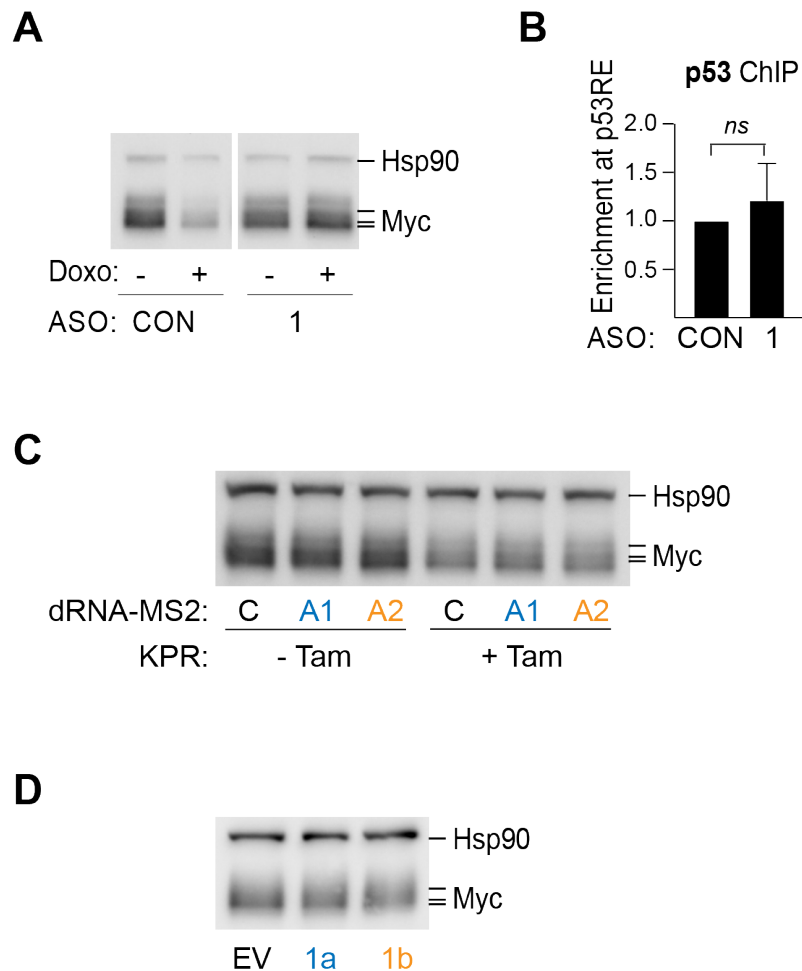
Figure S4. Effects of *Pvt1b* manipulation *in cis* and *in trans* on Myc protein levels, Related to Figure 4.

(A) Representative immunoblot analysis of Myc protein levels in whole-cell extracts isolated from ASO knockdown experiments in Fig. 4D. Hsp90 as a loading control.

(B) ChIP-qPCR analysis showing the enrichment of p53 binding at p53RE relative to input in CON- and ASO1- treated WT MEFs following 8 h Doxo treatment. Data represented mean ± - SEM of biological replicates, ns = not significant, paired t-test.

(C) Representative immunoblot analysis of Myc protein levels in whole-cell extracts isolated from CRISPRa experiments in Fig. 4H. Hsp90 as a loading control.

(D) Representative immunoblot analysis of Myc protein levels in whole-cell extracts isolated from exogenous overexpression experiments in Fig. 4L. Hsp90 as a loading control.

A *KPR* clone D

B *KPR* clone E

C

D
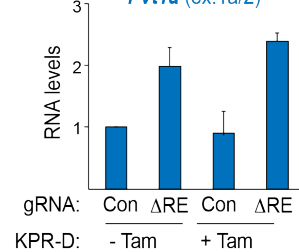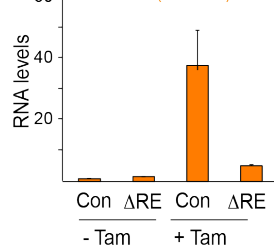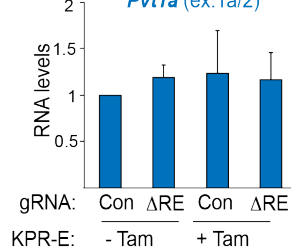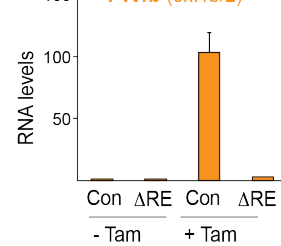
E
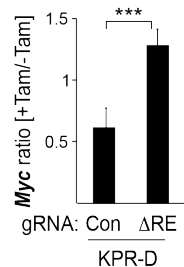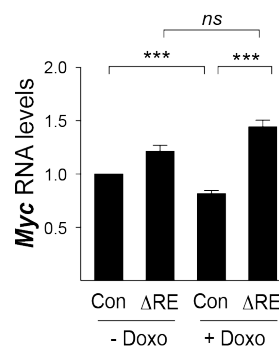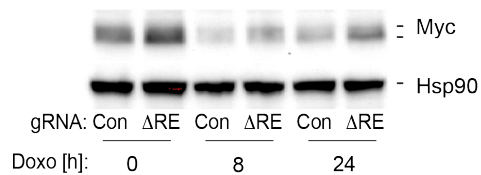

F
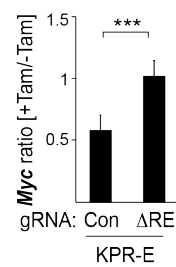
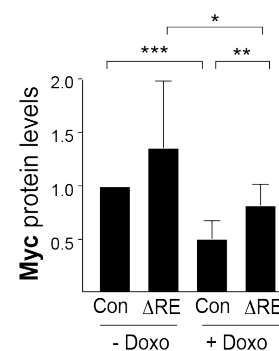

G *p53-proficient MEFs*
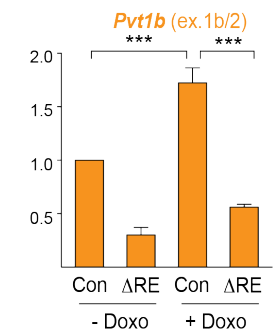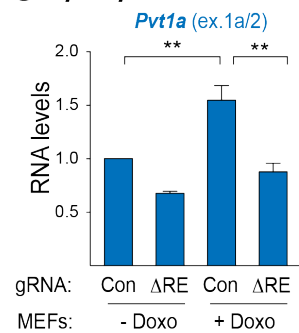
H

I

J

Figure S5. Genetic inhibition of *Pvt1b* rescues stress-dependent *Myc* repression in *KPR* clonal and MEF cell lines, Related to Figure 5.
(A-F) Analysis of (A, C, E) clone D and (B, D, F) clone E, isolated from *KPR* cells infected with a gRNA targeting the *Pvt1b* p53RE (ΔRE). As a control, *KPR* clones expressing Con gRNA were analyzed.
(A, B) Sanger sequencing of the region containing the *Pvt1b*-associated p53RE.
(C, D) qRT-PCR analysis of relative *Pvt1a* and *Pvt1b* RNA levels in indicated samples.
(E, F) qRT-PCR of the ratio (+Tam/-Tam) of *Myc* expression in indicated clones. Bars show the mean ± SEM of n=3 biological replicates, ***p<0.001, paired t-test.
(G-J) Analysis of MEF population cell lines, infected with a gRNA targeting the *Pvt1b* p53RE (ΔRE) or a non-targeting control (Con) and harvested untreated or 8-24 h post Doxo treatment.
(G) qRT-PCR analysis of relative *Pvt1a* and *Pvt1b* RNA levels in indicated samples. Data represent mean ± SEM of n=3 biological replicates, **p<0.01, ***p<0.001, paired t- test.
**(H)** qRT-PCR analysis of relative *Myc* RNA levels in indicated samples. Data represented as mean±SEM of n=3 biological replicates, ns = not significant, ***p<0.001, paired t- test.
(I) Immunoblot analysis of Myc protein levels in whole-cell extracts from indicated cells. Hsp90 as a loading control.
(J) Quantification of Myc protein levels from cells in (I). Data represent mean ± SEM of n=7 biological replicates, *p<0.05, **p<0.01, ***p<0.001, paired t- test.
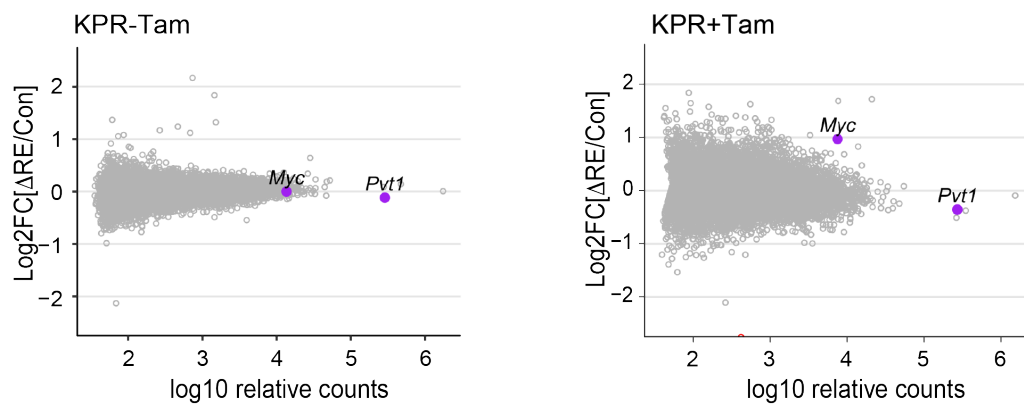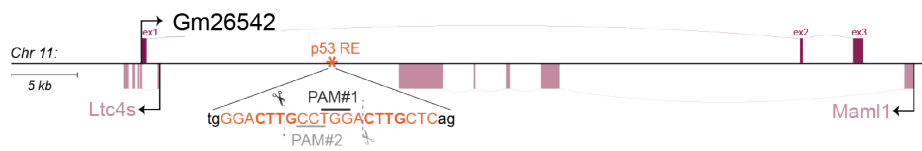
A
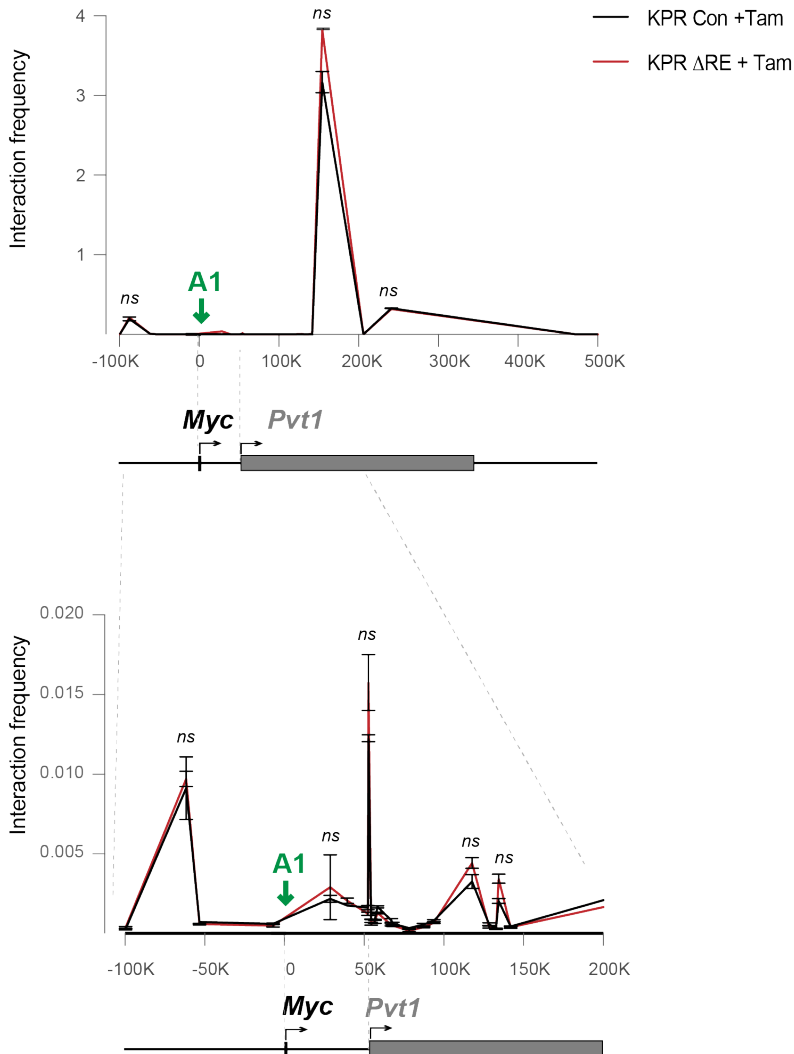
B

Figure S6. Effects of genetic inhibition of *Pvt1b* on the chromatin architecture of the *Myc-Pvt1* locus and *Myc* transcription, Related to Figures 5 and 6.

(A) 3C analysis in *KPR* cells, infected with *Pvt1b* p53RE-targeting (ΔRE) or Control (Con) gRNAs and treated for 24 h with Tam. Interaction frequency relative to an anchor in the *Myc* promoter (A1, green arrow) is plotted from three technical replicates from a representative experiment of two biological replicates, as described in Figure S2.

(B) MA plots from TT-TimeLapse-seq data depicting log2 fold change in nascent RNA (n >11,000 for each condition) in (A) untreated or (B) Tam-treated KPR cells. *Myc* and total *Pvt1* are indicated (purple dots).

A

Gm26542

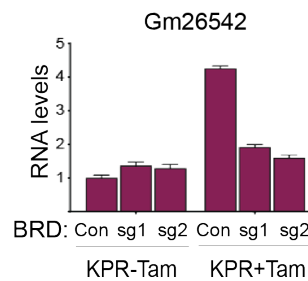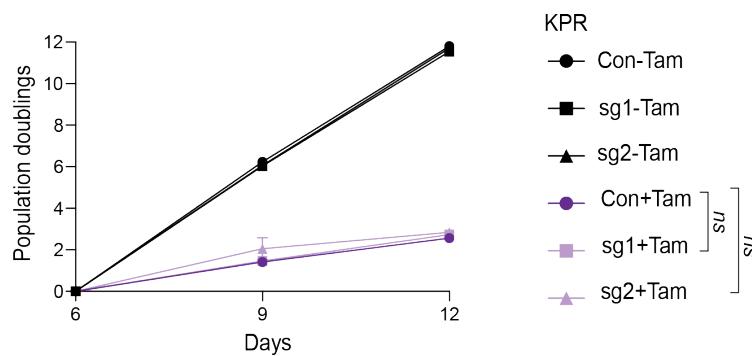Chr 11: ...Ltc4s... p53 RE ...ex2 ex3... Maml1

5 kb

PAM#1
tgGGA**CTTG**CC**T**GGA**CTTG**CTCag
PAM#2

B

p53RE: GGA**CTTG**CCTGGA**CTTG**CTC

GGA**CTT**t t**G**CCTGGA**CTTG**CTC
sg1   G - - - - - - - - - - - - -A**CTTG**CTC
      G - - - - - - - - - - - - -A**CTTG**CTC
      GGA**CT** - **G**CCTGGA**CTTG**CTC
sg2   - - - - - - - - - - - - - - - - **TG**CTC
      GGA**CTTG**CCTGGA - - **TG**CTC

C

Gm26542

RNA levels

BRD: Con sg1 sg2 | Con sg1 sg2
     KPR-Tam | KPR+Tam

D

Population doublings

6   9   12
Days

KPR
● Con-Tam
■ sg1-Tam
▲ sg2-Tam
● Con+Tam
■ sg1+Tam
▲ sg2+Tam

ns
ns

E

Relative tumor burden
[tumor area/total lung area]
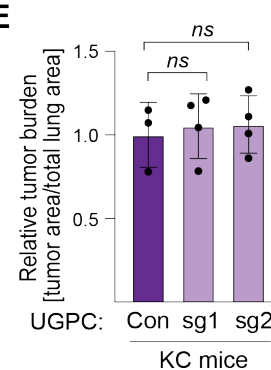
ns
ns

UGPC: Con sg1 sg2
KC mice

Figure S7. Mutagenesis of Gm26542-associated p53RE does not affect proliferation *in vitro*, tumor growth *in vivo*, Related to Figure 7.

(A) Schematic of the mouse Gm26542 lncRNA locus depicting the sequence of the p53RE located in intron 1, and the PAM sites (PAM #1 and PAM #2) utilized by guide RNAs sg1 and sg2, respectively.

(B) Sanger sequencing of the region containing the Gm26542-associated p53RE in *KPR* cells infected with sg1 or sg2.

(C) qRT-PCR analysis of relative RNA levels of the Gm26542 lncRNA in Con-, sg1- and sg2-infected *KPR* cell populations showing the p53-dependent induction of Gm26542 at 24 hours post Tam treatment and the abrogation of this induction by p53RE mutagenesis.

(D) Growth analysis showing population doublings in Con, sg1, or sg2 gRNA-expressing *KPR* cells, untreated or treated with Tam. Data show mean ± SEM of n=3 biological replicates, ns= not significant, unpaired t-test.

(E) Quantification of tumor burden as tumor area relative to total lung area in KC mice infected with indicated gRNAs and analyzed at 16 weeks post tumor initiation (pti) as described in Fig. 7. Data show tumor burden of individual mice and mean±SD, ns = not significant, unpaired t-test.